Water Resources Research

Key Points:
- A process-based model is developed to simulate mechanisms related to bank collapse in tidal channels
- A significant linear relation is present between bank height and the contribution of bank collapse to bank retreat for cantilever-shape bank
- Collapsed bank soil prevents further channel widening thus facilitating deepening and development of a convex-shape bank profile

Supporting Information:
- Supporting Information S1

Correspondence to:
Z. Gong,
gongzheng@hhu.edu.cn

The Role of Collapsed Bank Soil on Tidal Channel Evolution: A Process-Based Model Involving Bank Collapse and Sediment Dynamics

K. Zhao[1] , Z. Gong[1,2] , F. Xu[3] , Z. Zhou[1] , C. K. Zhang[1], G. M. E. Perillo[4], and G. Coco[5]

[1]State Key Laboratory of Hydrology-Water Resources and Hydraulic Engineering, Hohai University, Nanjing, China, [2]Jiangsu Key Laboratory of Coast Ocean Resources Development and Environment Security, Hohai University, Nanjing, China, [3]State Key Laboratory of Estuarine and Coastal Research, East China Normal University, Shanghai, China, [4]Instituto Argentino de Oceanografía (CONICET e UNS), Bahía Blanca, Argentina, [5]School of Environment, University of Auckland, Auckland, New Zealand

Abstract We develop a process-based model to simulate the geomorphodynamic evolution of tidal channels, considering hydrodynamics, flow-induced bank erosion, gravity-induced bank collapse, and sediment dynamics. A stress-deformation analysis and the Mohr-Coulomb criterion, calibrated through previous laboratory experiments, are included in a model simulating bank collapse. Results show that collapsed bank soil plays a primary role in the dynamics of bank retreat. For bank collapse with small bank height, tensile failure in the middle of the bank (Stage I), tensile failure on the bank top (Stage II), and sectional cracking from bank top to the toe (Stage III) are present sequentially before bank collapse occurs. A significant linear relation is observed between bank height and the contribution of bank collapse to bank retreat. Contrary to flow-induced bank erosion, bank collapse prevents further widening since the collapsed bank soil protects the bank from direct bank erosion. The bank profile is linear or slightly convex, and the planimetric shape of tidal channels (gradually decreasing in width landward) is similar when approaching equilibrium, regardless of the consideration of bank erosion and collapse. Moreover, the simulated width-to-depth ratio in all runs is comparable with observations from the Venice Lagoon. This indicates that the equilibrium configuration of tidal channels depends on hydrodynamic conditions and sediment properties, while bank erosion and collapse greatly affect the transient behavior (before equilibrium) of the tidal channels. Overall, this contribution highlights the importance of collapsed bank soil in investigating tidal channel morphodynamics using a combined perspective of geotechnics and soil mechanics.

1. Introduction

Tidal channels are one of the most distinctive features of tidal systems (D'Alpaos, 2005; Perillo, 2009). The landward part of a tidal channel is usually covered by halophytic vegetation that is regularly submerged during high tide (Allen, 2000). The seaward part is instead characterized by bare flats with the elevation comprised between the low and high tidal water levels (Friedrichs, 2011). Tidal channels are the skeleton of the circulatory system through which water, sediment, organic matter, nutrients, and pollutants are transported in and out of wetlands, thus determining the evolution and functioning of the overall system (Lanzoni, 2002; Lanzoni & D'Alpaos, 2015; Perillo, 2009; van Maanen et al., 2015). Tidal channels provide extensive ecosystem functions serving, for example, as habitats of migratory birds and benthos species, and accommodating commercially important fisheries (Barbier et al., 2011; Coco et al., 2013; Fagherazzi et al., 2012; van der Wegen & Roelvink, 2008).

The equilibrium configurations of tidal channels have been initially investigated using empirical or semiempirical relations. The seminal work relating the cross-sectional area, A, to the tidal prism, P (i.e., P-A relationships) was conducted by O'Brien (1931) and Jarrett (1976). Friedrichs (1995) theoretically developed a similar relation using the peak spring discharge, Q, to represent the tidal forcing (i.e., Q-A relation). The linear relation was further studied and extended by D'Alpaos et al. (2010) and Xu et al. (2017). Following studies of river morphodynamics (Ikeda et al., 1988; Parker, 1978; Pizzuto, 1990), a novel process-based cross-sectional model was proposed by Fagherazzi and Furbish (2001) focusing on the morphodynamic evolution of salt marsh channels and the associated adjacent platform. This cross-sectional model was then applied to tidal channels on unvegetated tidal flats (Lanzoni & D'Alpaos, 2015; Xu et al., 2019). More
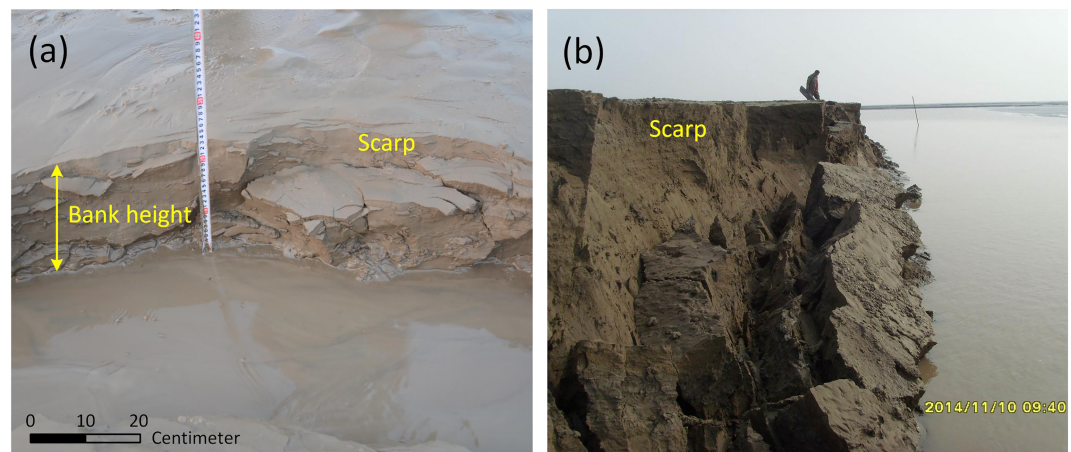
Figure 1. Photos of (a) small-scale and (b) large-scale bank collapse of tidal channels in the middle part of the Jiangsu coast (China).

recently, morphodynamic models able to couple a number of additional processes, for example, wind waves, consolidation, and bank erosion, have been employed to study the morphodynamic evolution of tidal flats and channels (e.g., van der Wegen et al., 2008; Zhou, van der Wegen, et al., 2016; Zhou, Ye, et al., 2016). However, few studies and models take into account bank collapse from a combined perspective that includes geotechnical and soil mechanic dynamics. Observations (e.g., Ginsberg & Perillo, 1990) show that the flow-induced bank erosion and subsequent bank collapse often occur in tidal channels resulting in rapid morphological changes over the whole flat channel system (Figure 1).

With respect to bank collapse in tidal environments, Van Eerdt (1985) evaluated the stability of cantilever-shape salt marsh cliffs on the basis of beam failure analysis. Ginsberg and Perillo (1990) reported the origin and development of erosional cuspate shapes, showing that large slope angle is the main cause for the slumping of the tidal channel bank. They also considered that dynamic processes such as tidal currents and short wind waves affect the formation of these cuspate erosional features. Gabet (1998) further suggested that the persistence of collapsed bank material in salt marsh channels accounts for the "channel erosion paradox," namely, the tendency of salt marsh channels to migrate laterally at small rates despite the widespread occurrence of bank collapse. The role of roots and consolidation on bank stability was highlighted by Chen et al. (2012), demonstrating that the stability of the upper bank is a function of roots, while consolidation primarily affects the lower part. In order to illustrate the sediment exchanges between salt marsh channel and the associated adjacent platform, some idealized numerical models were proposed applying a linear relation linking soil creep with bed slope and soil diffusivity (Kirwan & Murray, 2007; Larsen et al., 2007; Mariotti et al., 2016). Although able to reproduce the bank retreat process, the diffusive model does not address the physical mechanisms related to bank collapse. In recent years, several models were developed taking into account bank collapse from a combined perspective of geotechnical and soil mechanic dynamics. Using laboratory experiments, Francalanci et al. (2013) and Bendoni et al. (2014) studied toppling failure induced by wind waves in salt marshes. Their analysis indicated that the most critical conditions triggering marsh bank collapse depend on the presence of water inside the tension crack and low water levels in front of the bank. Applying stress-deformation analysis, Gong et al. (2018) demonstrated that bank failure process can be categorized into three stages, that is, shear failure (SF) at the bank toe (Stage I), tensile failure (TF) on the bank top (Stage II), and sectional cracking from the bank top to the toe (Stage III). The contribution of bank collapse to bank retreat was also shown to be as high as 85%, indicating that the widening of tidal channels can in fact be dominated by bank collapse.

Bank collapse in fluvial system has been investigated using both physical experiments and numerical models (Fox & Wilson, 2010; Rinaldi & Darby, 2007). Some of the physical experiments focused on the role of external forcing on bank instability, for example, seepage flow (Karmaker & Dutta, 2013; Lindow et al., 2009), water level change (Nardi et al., 2012), and lateral fluvial erosion (Patsinghasanee et al., 2018). Other experiments analyzed the effects of bank morphology (e.g., bank height and angles) and soil

properties on bank stability (Fox & Felice, 2014; Nardi et al., 2012; Samadi et al., 2011). In terms of numerical models, two methods, namely, the limit equilibrium method and the stress-deformation analysis, have been proposed to study riverbank stability and resultant feedbacks with river morphology (see Gong et al., 2018, for more details). Following Gong et al. (2018), the stress-deformation analysis is applied in this study.

Large blocks, or chunks of soil, are deposited at the bank toe when bank collapse occurs. The collapsed bank soil temporarily protects bank material from direct flow-induced bank erosion and is gradually eroded by either waves or currents. The protecting effects are commonly implemented by placing the collapsed bank soil into a "black box," with no topographic expression, but making the sediment available for preferential scour by flow-induced bank erosion (Lai et al., 2015; Langendoen, 2000). The black box approach explicitly accounts for the protection provided by the collapsed soil and satisfies mass conservation. However, few studies attempt to explore the role of collapsed bank soil on the morphodynamic evolution of tidal channels. Here we present a process-based geomorphodynamic model based on Gong et al. (2018), coupling tidal flow, flow-induced bank erosion and resultant gravity-induced bank collapse, sediment transports, and bed level updating. The objectives of the present study include (1) analyzing the influences of bank height on bank collapse patterns and resultant contribution of bank collapse to bank retreat, (2) investigating the role of collapsed bank soil on the equilibrium configuration of tidal channels, and (3) gaining insight into the characteristics of the tidal channel cross section (CS) and comparing it with natural systems.

2. Methodology

We build on the Gong et al.'s (2018) bank retreat work to develop a more general morphodynamic model. The hydrodynamic, flow-induced bank erosion and bank collapse modules have been documented in detail by Gong et al. (2018). Here we only introduce the morphodynamic module (including bed level updating and sediment transports) and show the differences with Gong et al. (2018). A brief introduction of flow-induced bank erosion and bank collapse module is provided in Text S4 in the supporting information.

The interface between tidal flats and channel is sometimes abrupt, and bank height is defined as the height of the scarp (Figure 1a). Since sediment erosion and deposition are taken into account, the bank height is constantly changing. Twenty nodes are evenly distributed from bank top to the toe with an interval of $BH/20$ (BH is the bank height) to calculate flow-induced bank erosion and to update bank profiles (Figure 2c).

The tide-induced bed shear stress τ_b is estimated as

$$\tau_b = \frac{\rho_w g \overrightarrow{v} |v|}{C_z^2},$$ (1)

where ρ_w is the density of seawater (kg/m^3), g is the gravitational acceleration (m/s^2), $\overrightarrow{v}$ is the flow velocity in y direction (m/s), $|v|$ is the magnitude of the flow velocity in y direction (m/s), and C_z is the Chezy resistance calculated from Manning's formula (m$^{1/2}$/s). Variables are summarized in Text S1 in the supporting information.

2.1. Morphodynamic Module
2.1.1. Bed Level Update
Conservation of sediment is described:

$$(1-\varepsilon_p)\frac{\partial z_b}{\partial t} = \frac{f_M}{\rho_s}\left(Q_d - Q_e - Q_b + \frac{M_{cl}}{\Delta x \cdot \Delta y \cdot \Delta t}\right),$$ (2)

where z_b is bed elevation (m), t is time (s), f_M is morphological factor, ρ_s is the density of sediment without porosity which is set to 2,650 (kg/m^3), ε_p is bed porosity, which is set to 0.43 following Zhou, Ye, et al. (2016). Q_e and Q_d are respectively bed erosion and deposition fluxes described in detail in section 2.1.2. Q_b is the sediment flux resulting from bank retreat (kg/m^2/s), M_{cl} is the mass of collapsed bank material translated into channel bed (kg), Δt is the time step (s), and Δx and Δy represent respectively the size of the hydrodynamic mesh in the x and y directions (m). Both Q_b and M_{cl} will be described in detail in section 2.1.3.

The hydrodynamics have a timescale much faster than the morphodynamic one so that the bed evolution can be scaled up using a morphological factor (f_M) to accelerate the simulation (Roelvink, 2006).
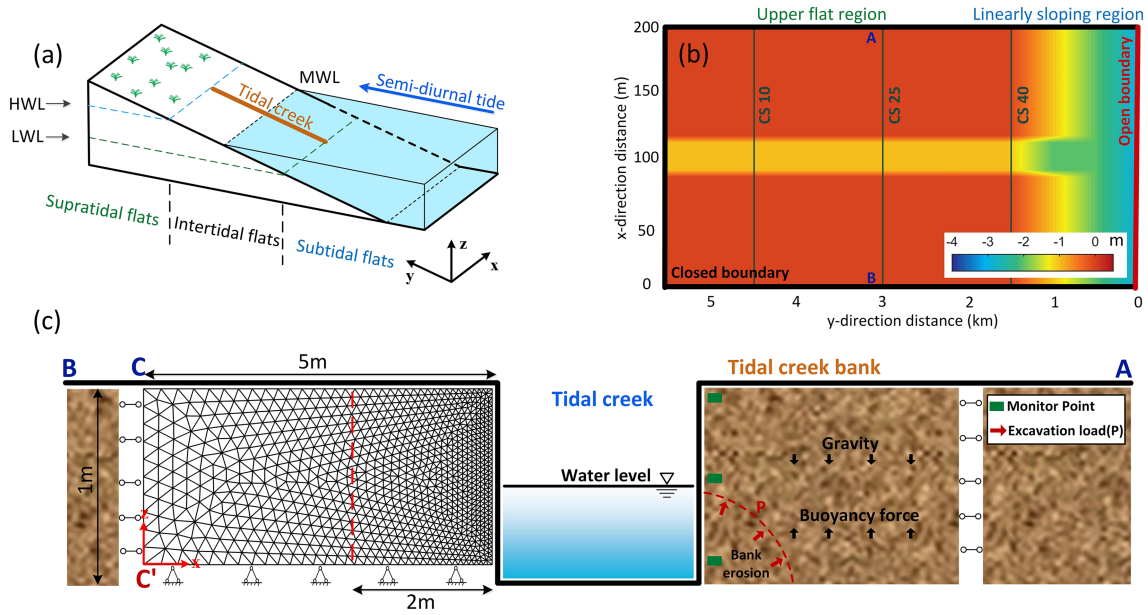
Figure 2. (a) Schematized model of tidal flats dissected by a tidal channel. (b) Initial bathymetry used for the simulations showing boundary conditions. Fifty cross sections (CS) are set with an interval of 100 m along the tidal channel. (c) Schematic profile view of tidal channel bank (A-B cross section in Figure 2b), showing the position of monitor points and external load (i.e., gravity, excavation load, and buoyancy force) and the mesh discretization and configuration of the simulation domain of the bank collapse module (modified from Gong et al., 2018). MWL = mean water level.

However, this approach is not feasible when dealing with bank collapse, which is instantaneous event. Therefore, we set the morphological factor to 10, but we set it to 1 when bank collapse occurs. Every time step before updating bed level, we check the occurrence of bank collapse for each cross section. If no bank collapse occurs, the morphological factor is set to 10; otherwise, the morphological factor is set to 1.

2.1.2. Sediment Transport Formulation

Bed load transport is neglected at this stage of research, in order to more insightfully separate the effects of bank collapse on morphological changes. Suspended sediment transport is simulated using two-dimensional advection-diffusion equation:

$$\frac{\partial (ch)}{\partial t} + \frac{\partial (uch)}{\partial x} + \frac{\partial (vch)}{\partial y} = \frac{\partial}{\partial x}\left(h\cdot K_x\cdot\frac{\partial c}{\partial x}\right) + \frac{\partial}{\partial y}\left(h\cdot K_y\cdot\frac{\partial c}{\partial y}\right) - Q_d + Q_e + Q_{be}, \tag{3}$$

where t is time (s), x and y are the Cartesian coordinates (m), c is the depth-averaged suspended sediment concentration (kg/m^3), h is the water depth (m), u and v are flow velocity in the x and y directions (m/s), K_x and K_y are the eddy diffusivities of suspended sediment (m^2/s), Q_{be} is the sediment flux resulting from flow-induced bank erosion described in detail in section 2.1.3 (kg/m^2/s), and Q_e and Q_d are respectively bed erosion and deposition fluxes (kg/m^2/s) described by the widely adopted Partheniades-Krone formulations (Krone, 1962; Partheniades, 1965):

$$Q_e = \begin{cases} M_e\left(\frac{\tau_b}{\tau_e}-1\right), & \text{if } \tau_b > \tau_e, \\ 0, & \text{if } \tau_b \leq \tau_e, \end{cases} \tag{4}$$

$$Q_d = \begin{cases} w_s c\left(1-\frac{\tau_b}{\tau_d}\right), & \text{if } \tau_b < \tau_d, \\ 0, & \text{if } \tau_b \geq \tau_d, \end{cases} \tag{5}$$

where M_e is the erosion parameter (kg/m^2/s), τ_e is the critical shear stress for bed erosion (Pa), w_s is the settling velocity (m/s), and τ_d is the critical shear stress for bed deposition (Pa).
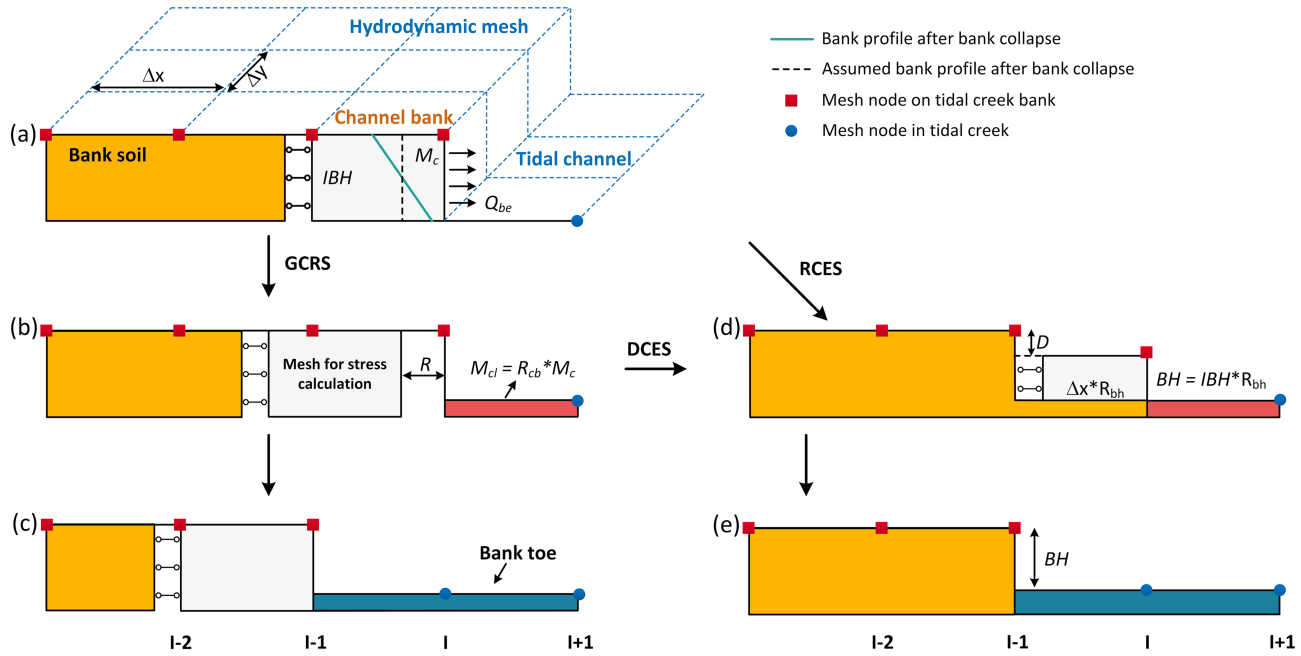
Figure 3. Illustration of the different schemes of coupling between the hydrodynamic module, bank erosion module, and bank collapse module. Panels (a)–(c) show the procedure of "ghost-cell retreat" scheme (GCRS), and (a), (d), and (e) demonstrate the procedure of "ghost-cell retreat converted to dry-cell erosion" scheme (RCES); (b) and (d) show the procedure of "dry-cell erosion" scheme (DCES); Δy and Δx represent the size of the hydrodynamic mesh in the longitudinal and latitudinal direction, respectively. R indicates the cumulative bank retreat distance, and D is the equivalent decrease in bank elevation for the bank retreat distance, R. M_c represents the mass of the collapsed bank soil. M_{cl} represents the mass of the collapsed bank soil translated into channel bed. R_{cb} represents the ratio between the collapsed bank material translated into channel bed and the whole collapsed material. Q_{be} is the sediment flux resulting from flow-induced bank erosion. IBH is the initial bank height set to 1 m, and BH is bank height. The hinged support is the same as Figure 2c. We refer the reader to sections 2.2.1 and 2.2.2 for more details about the computational domain of the bank collapse module (i.e., the geotechnical mesh).

2.1.3. Flow-Induced Bank Erosion and Collapse

The occurrence of flow-induced bank erosion leads to an increase in suspended sediment concentration. On the basis of mass conservation, the overall sediment flux resulting from flow-induced bank erosion is simulated as

$$Q_{be} = \frac{\varepsilon \cdot \min\{h, BH\} \cdot \rho_{bank}}{\Delta x} \tag{6}$$

where ε is the bank retreat rate resulting from flow-induced bank erosion (m/s) calculated from equation S3, see Text S3 in the supporting information; h is water depth (m); BH is bank height (m); ρ_{bank} is the density of bank soil (kg/m³); and Δx represents the size of the hydrodynamic mesh in the x direction (m). If there is no collapsed bank soil, Q_{be} is eroded from the intact bank. Otherwise, Q_{be} is eroded from the collapsed bank soil.

The collapsed bank soil is divided into two parts according to the ratio between the collapsed bank material translated into channel bed and the whole collapsed material (R_{cb}, see Figures 3a and 3b):

$$\begin{cases} M_{cp} = (1 - R_{cb}) \cdot M_c, \\ M_{cl} = R_{cb} \cdot M_c, \end{cases} \tag{7}$$

where M_{cp} is the mass of the collapsed bank soil protecting bank from bank erosion (kg) and M_c is the mass of the collapsed bank soil (kg), calculated according to the potential failure plan and bank height (Figure 3a). M_{cl} is the mass of the collapsed bank soil translated into channel bed (kg). When bank collapse occurs, the elevation of the adjacent channel bed increases according to M_{cl} (Figure 3d).

R_{cb} is a function of soil type (cohesive or noncohesive sediment), flow intensity, and the duration of air exposure and certainly varies along the tidal channel. For the sake of simplification, R_{cb} is set to a constant along the tidal channel.

Bank retreat rate decreases under the protection of collapsed bank soil. Following Langendoen (2000) and Lai et al. (2015), the protection effects are implemented by replacing bank retreat with the loss in the collapsed bank soil, M_{cp} (i.e., Q_{be} is sometimes eroded from the collapsed bank soil). Therefore, Q_b, used to calculate bank retreat distance (see equation (2) and section 2.2.2), is calculated as

$$Q_b = \begin{cases} 0 & \text{if } M_{cp} \geq Q_{be} \cdot \Delta t \cdot \Delta x \cdot \Delta y, \\ Q_{be} - \dfrac{M_{cp}}{\Delta t \cdot \Delta x \cdot \Delta y} & \text{if } M_{cp} < Q_{be} \cdot \Delta t \cdot \Delta x \cdot \Delta y, \end{cases} \tag{8}$$

where Q_b is the sediment flux resulting from bank retreat ($kg/m^2/s$). It should be noted that Q_b is used to calculate bank retreat distance (equation (2)), while Q_{be} is used to simulate the increase in suspended sediment concentration (equation (3)). The effects of the collapsed bank soil are implemented as follows. First, the mass of sediment in the black box (M_{cp}) is translated to sediment flux according to the size of the hydrodynamic mesh and time step (see section 1). Then, we check whether $M_{cp}/(\Delta x \cdot \Delta y \cdot \Delta t)$ is larger than Q_{be}; if so, protection effects are dominating, and we can assume that Q_b is equal to 0 (i.e., no bank retreat is present).

2.2. Numerical Approach

Since the discrete mesh and numerical solver applied to simulate hydrodynamics has been documented in detail by Gong et al. (2018), we have omitted it from this section. The transformation of effective shear stresses in the momentum equations and drying or flooding procedures are described in the supporting information Text S2.

2.2.1. Bank Collapse

The initial computational domain of the bank is 5 m in the transverse and 1 m in the vertical direction (Figure 2c). The domain is discretized by means of triangular mesh with higher resolution close to the bank edge (Figure 2c). Since the bank height varies during the simulation, we should ideally apply mesh self-discretization and dynamic self-adjustment of the computational domain. However, mesh self-discretization, especially for unstructured cells, is complex and computationally costly (Chew, 1989). Here we propose a simple but efficient method, using the meshes of the initial bank to account for the variation of bank height. R_{bh} is defined as the ratio of present bank height to the initial bank height. For an arbitrary tidal channel bank, the computational domain is $5 * R_{bh}$ m in the transverse direction and $1 * R_{bh}$ m in the vertical direction (Figure 3d). Using a regular mesh discretization has two advantages. First, the mesh discretization pattern of each channel bank is identical; thus, the bank height only affects the resolution of the stress distribution. Since the finite element method is highly affected by mesh discretization, the identical mesh pattern ensures the regularity of model results. Second, this method saves computational time and avoids probable inaccuracy induced by mesh self-discretization and dynamic self-adjustment of the computational domain.

The lower edge of the bank is set to a nondeformation boundary in both horizontal and vertical directions, and the left edge (i.e., C-C′ in Figure 2c) is fixed in the horizontal direction but is allowed to deform vertically. Once bank collapse occurs, the domain of the bank is redefined to guarantee that the computational domain of the bank collapse module remains $5 * R_{bh}$ m in the transverse and $1 * R_{bh}$ m in the vertical direction.

2.2.2. Module Coupling

To our knowledge, existing approaches describing the process of tidal channel bank retreat, include the "dry-cell erosion" scheme (DCES) and "ghost-cell retreat" scheme (GCRS). DCES is used in many studies (van der Wegen et al., 2008; van der Wegen et al., 2010), allowing the (partial) redistribution of an erosion flux from a wet cell to the adjacent dry cells (Deltares, 2014). Based on the cut-cell/ghost-cell method, which is commonly used for complex geometries (Canestrelli et al., 2016), GCRS was first put forward by Gong et al. (2018), simulating bank retreat according to the value of the bed shear stress at the bank. Contrary to DCES in which bank retreat is replaced with a decrease in bank height, GCRS physically describes bank retreat processes (see Figures 3a–3c). The advantages and disadvantages of both methods are summarized in Table 1. To better simulate the process of bank retreat, a new approach merging DCES with GCRS is proposed, namely, "ghost-cell retreat converted to dry-cell erosion" scheme (RCES). When bank collapse occurs, the new bank profile (green line in Figure 3a) is assumed to be vertical (black dashed line) on the basis of mass conservation. The retreat distance and the mass of the collapsed bank soil are then calculated based on the potential failure plan. In terms of GCRS, the retreat distance R is recorded, and the

Table 1
Advantages and Disadvantages of DCES, GCRS, and RCES

Approach	Advantages	Disadvantages
DCES van der Wegen et al. (2008)	Instantaneous feedback to flow field No limitation related to mesh size Mass conservation	Neglects bank collapse
GCRS Gong et al. (2018)	Consider bank collapse	Intermittent feedback to flow field Requires small size of meshes
RCES This research	Instantaneous feedback to flow field Consider bank collapse No limitation related mesh size Mass conservation	Underestimates bank retreat rate

Note. DCES = "dry-cell erosion" scheme; GCRS = "ghost-cell retreat" scheme; RCES = "ghost-cell retreat converted to dry-cell erosion" scheme.

computational domain of bank collapse is redefined (Figure 3b). The channel cross-sectional area (or width) varies intermittently, since the hydrodynamic mesh remains unchanged until the cumulative retreat distance R reaches the transverse size of the hydrodynamic mesh Δx (Figures 3b and 3c). However, the eroded and collapsed bank soil continuously deposits in front of the bank. In order to ensure mass conservation, GCRS commonly requires that the transverse size of the hydrodynamic mesh is as small as possible. In terms of RCES, the retreat distance R is replaced with a decrease in bank height D on the basis of mass conservation (similar to DCES). At the same time, part of the collapsed bank soil (M_{cl}) deposits at the bank toe directly increasing the elevation of the adjacent channel bed (Figure 3d). The computational domain of the bank collapse module and the associated geotechnical mesh is redefined (see section 2.2.1 for more details). When bank height decreases to 0, the mesh nodes used to calculate bank height is changed (e.g., using I and I + 1 in Figure 3d and using I − 1 and I in Figure 3e). This treatment guarantees mass conservation and feeds back instantaneously onto the flow field but underestimates bank retreat rate since bank stability is related to bank height. Other advantages and disadvantages of RCES are shown in Table 1.

2.3. Model Setup

The model geometry includes an upper flat region and a linearly sloping lower region with an initial bed slope of 0.2% (Gong et al., 2017; Xu et al., 2017). The computational domain of the hydrodynamics is 5,500 m long and 200 m wide. In the upper flat region, a straight tidal channel is present with the following characteristics: 4 km long, 20 m wide, and 1 m deep (Figure 2b). It should be noted that tidal channels rarely begin as shallow trapezoidal trenches that then deepen and widen. We simplify the initial topography to directly shed light on the effects of collapsed bank soil on tidal channel evolution. The model area for the flow is discretized using uniform rectangular cells with a size of 20 m in the longitudinal and 5 m in the latitudinal directions. The seaward boundary is imposed as a sinusoidal semidiurnal tide with a range of 2 m. The Manning's coefficient is set to 0.026 s/m$^{1/3}$ (van der Wegen et al., 2008), and the value of the eddy viscosity, ν_e, is 1.0 m^2/s, based on previous studies (van der Wegen et al., 2008; Zhou et al., 2014). The hydrodynamic time step is set to 6 s to satisfy both the Courant stability and horizontal viscosity term condition.

The erosion and failure of channel banks are assumed to be isotropous within 100 m in the longitudinal direction; thus, the tidal channel is divided into 50 segments. The CS is set in the middle of a segment with an interval of 100 m along the tidal channel.

The soil-related parameters are listed in Table 2 and are based on previous studies (Hanson & Simon, 2001; Lai et al., 2015; Simon & Thomas, 2002). Several numerical experiments on channel evolution are performed (Table 3), with the aim to separate individual processes: (1) without considering bank erosion and collapse; (2) without considering bank collapse; (3) considering both bank erosion and collapse; (4) changing the critical shear stress for bank erosion, τ_{be}; and (5) changing the ratio of collapsed bank soil translated into channel bed, R_{cb}. In the remaining of the manuscript, Run A represents case without considering bank erosion and collapse, Run B represents case without considering bank collapse, and Run C represents case taking into account both bank erosion and collapse.

Table 2
Parameter Values Applied in This Research

Parameters	Units	Default value
Hydrodynamic module		
Horizontal eddy viscosity, v_e	m/s^2	1.0
Manning's coefficient, n	$s/m^{1/3}$	0.026
Flow-induce bank erosion module		
Erodibility coefficient for bank erosion, k	$m^3/N/s$	8×10^{-7}
Critical Shear Stress for bank erosion, τ_{be}	Pa	0.062
Bank collapse module		
Effective friction angle, φ'	o	28.6
Effective cohesion, c'	kPa	4.5
Saturated unit weight, γ_{sat}	kN/m^3	19.4
Elastic modulus, E	MPa	5.0
Poisson's ratio, μ	(–)	0.38
Reduction factor, k_{re}	(–)	0.1
Morphodynamic module		
Eddy diffusivities of suspended sediment, K_x, K_y	m^2/s	10
Erosion parameter for bed erosion, M_e	$kg/m^2/s$	5×10^{-5}
Critical Shear Stress for bed erosion, τ_e	Pa	0.5
Critical Shear Stress for bed deposition, τ_d	Pa	1,000
Settling velocity, w_s	m/s	5×10^{-4}
Bed porosity, ε_p	(–)	0.43
Ratio of collapsed bank soil translated into channel bed, R_{cb}	(–)	0.5

Table 3
Values of the Relevant Parameters Adopted in Each Case (Parameters Not Listed Are Same as in Table 2)

Run ID	τ_{be}	R_{cb}	Notes
	(Pa)	(–)	
A	(–)	(–)	Without bank erosion and collapse
B1	0.062	(–)	Without bank collapse
B2	0.125	(–)	
B3	0.25	(–)	
C1	0.062	0.5	With both bank erosion and collapse
C2	0.125	0.5	
C3	0.25	0.5	
C4	0.062	0.1	
C5	0.062	0.3	
C6	0.062	0.8	

3. Results

3.1. Model Validation

Using a physical model with internal dimensions (Length × Height × Width) of 2 × 1 × 1 m, Samadi et al. (2013) investigated the process of bank collapse resulting from artificial undermining. In their experiments, six overhanging banks composed of silt and clay, respectively, were considered. The size (Length × Height × Width) of the banks was 1 × 0.8 × 1 m, and the geotechnical parameters of each bank are listed in Table 4. Since the fluvial erosion process is replaced with the artificial undermining, the consideration of the transformation between saturated and unsaturated soil is neglected.

The bank length is 1 m in physical experiments and 4 m in numerical simulations, in order to reduce the influence of the lateral boundary on stress distribution (i.e., CC′ in Figure 2c). The mesh discretization is realized using the meshes of the initial bank multiplied by $R_{bh} = 0.8$ (more details are provided in section 2.2.1). Given that clay is stronger under tensile than silt, the reduction factor k_{re} is set to 0.2 for clay but 0.1 for silt. Other geotechnical parameters are set according to Table 4.

Figure 4 shows the reproduced failure zone of each experiment, and a comparison between the observed and simulated failure planes. The observed failure planes in all six tests pass through the simulated TF zone and meet nearly at the middle of the TF zone on the bank top. In the context of clay-composed bank with low cohesion (or low dry density), the predicted failure plane well agrees with the observed failure plane (Figure 4a). The goodness of fit between the predicted and observed failure plane becomes high with the decrease in soil cohesion (Figures 4a–4c). For banks composed of silt, the predicted failure plane does not fit with the observed failure plane, and the observed failure volume is larger than the predicted failure volume (Figures 4d–4f). With the increase in soil cohesion, the failure volume and the required undermining width (UW) to trigger bank collapse increase. Also, the area of SF zone decreases with increase in soil cohesion.

The percentage contribution of bank collapse to bank retreat, C_{bc}, has been calculated from numerical and physical models and is shown in Table 4 (the calculation method of C_{bc} is provided in Text S4 in the supporting information). The calculated C_{bc} from numerical model corresponds well to the one observed from laboratory experiments. The C_{bc} of a silt-composed bank is larger than the C_{bc} of a clay-composed bank, indicating that clay-composed bank is more stable than silt-composed bank.

3.2. Effects of Collapsed Bank Soil on Bank Collapse Patterns and C_{bc}

A typical CS (CS 40, see Figure 2b) near the transition between the upper flat region and the linearly sloping lower region is chosen, and the failure processes of the tidal channel bank with different bank height are shown in Figure 5. According to the expansion of the failure region resulting from flow-induced bank erosion, both failure processes can be categorized into three stages.

In the context of bank collapse with small bank height (e.g., bank height = 0.4 m, Figure 5a), the major principal effective stress σ_1' is focused on the right lower part of the bank (i.e., bank toe) at the initial stage, while the minor principal effective stress σ_3' shows a significant decrease (see Gong et al., 2018, for the concept detailed description of the principal effective stress, shear and tensile failure). Since the excavation load directly relates to the principal effective stress, the external force exerted to the rest of the bank after flow-induced bank erosion is smaller in the case of small bank height (a detailed explanation of the excavation load

Table 4
Geotechnical Parameters of Remodeled Overhanging Banks in Samadi et al. (2013) and C_{bc} Calculated From Laboratory and Numerical Model Respectively

Test	Soil class	Dry density (g/cm^3)	Cohesion (kPa)	Internal friction angle (^{o})	Elastic modulus (MPa)	Poisson's ratio (–)	C_{bc} from Lab (%)	C_{bc} from Num (%)
a	Clay	1.5	6.0	15.0	1.2–2.4	0.32–0.4	85.2	85.54
b		1.7	14.0	16.5	1.8–5.0	0.32–0.4	83.97	82.79
c		1.8	17.0	17.0	2.4–8.0	0.32–0.4	83.57	79.84
d	Silt	1.4	2.0	18.0	4.0–7.0	0.30–0.36	97.29	94.9
e		1.5	2.5	21.5	6.0–8.0	0.30–0.35	96.47	90.42
f		1.6	4.5	24.0	8.0–10.0	0.33–0.43	87.6	84.29

is provided in Text S4 in the supporting information). During Stage I, in the middle of the bank just below the cantilever, σ_3' drastically decreases below the critical tensile strength resulting in a local tensile failure (TF). This is in line with previous experiments (Samadi et al., 2011; Samadi et al., 2013) where tension cracks are observed just below the cantilever and part of the soil detaches from the bank under gravity. Close to the bank toe, both σ_1' and σ_3' decrease slightly without the occurrence of shear failure (SF). On the bank top, σ_3' decreases to a negative value, while local σ_1' increases sharply. During Stage II, σ_3' on the bank top decreases below the critical tensile strength leading to TF. Since soil is no longer able to withstand tension, the TF region expands further downward. Although σ_1' increases at the bank toe, the magnitude of σ_1' is still too small to trigger SF. At this stage, TF occurs at the bank top, while the bank toe is stable. During Stage III, cracking appears from the bank top to the toe, ultimately leading to the occurrence of
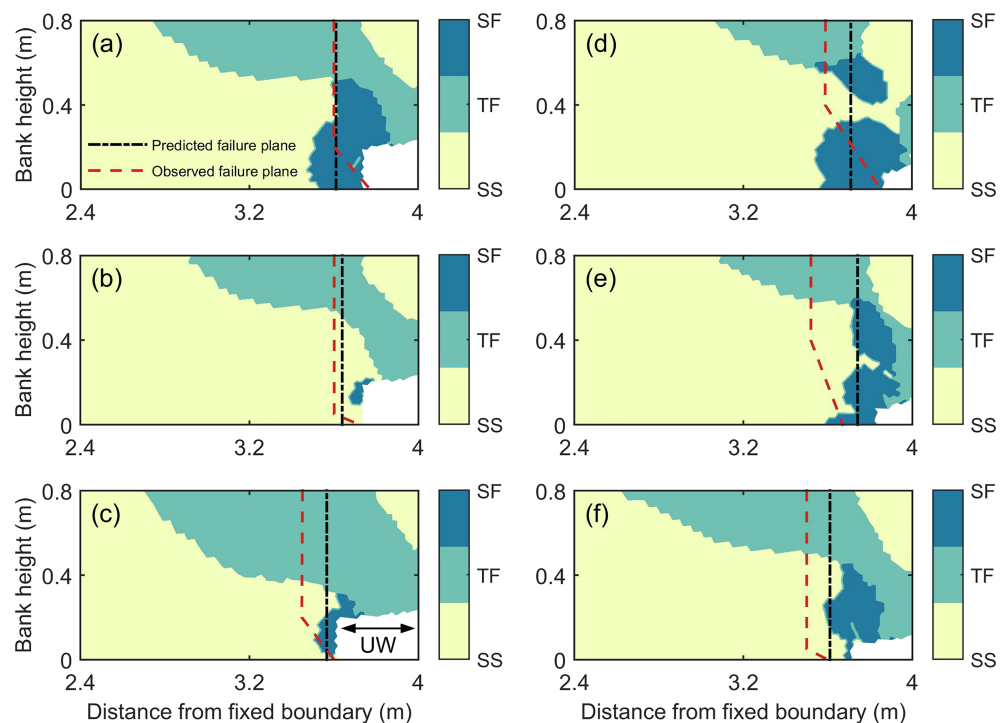

Figure 4. Reproduced failure zone of experiments conducted in Samadi et al. (2013). Panels (a)–(f) refer to Tests a–f in Table 4, respectively. Since the failure region is characterized by tensile failure, we assume that the failure plane is vertical and we calculate the new position of the bank using volume conservation. The black dash-dotted line represents the predicted failure plane from the numerical model, and the red dashed line indicates the observed failure plane from laboratory experiments in Samadi et al. (2013). SS indicates stable state, TF indicates tensile failure, and SF indicates shear failure. UW is the undermining width.
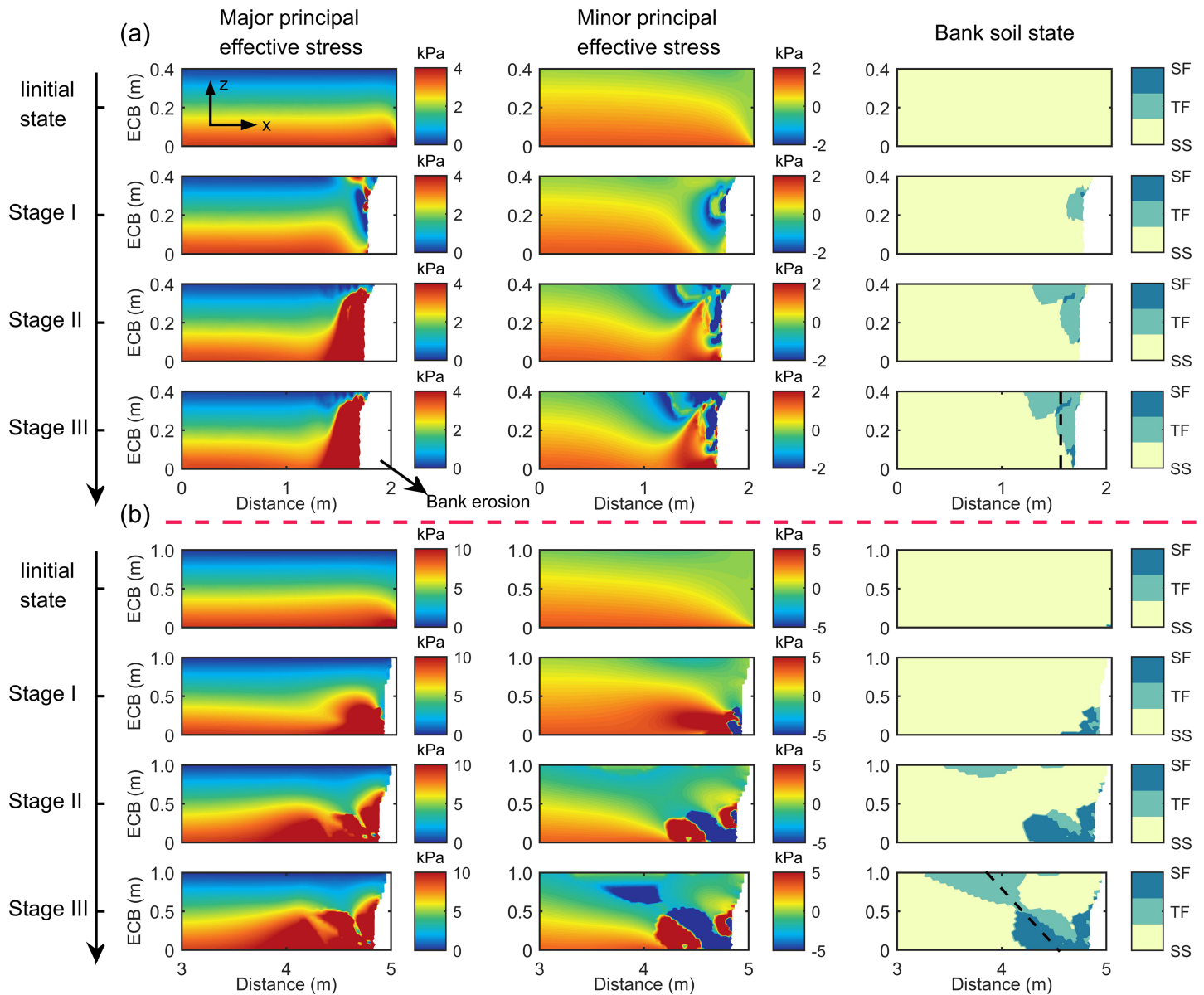
Figure 5. Variations of major and minor principal effective stress and bank soil state for bank with different bank height (a) bank height = 0.4 m and (b) bank height = 1 m. Given the limited effects of flow-induced bank erosion, stress distribution on the right side of the red dashed line in Figure 2c is shown. Black dashed line represents the potential failure plan (bottom right panel). The x and z directions are consistent with those in Figure 2. The vertical axis ECB represents elevation with respect to channel bottom in front of the bank. SS indicates stable state, TF indicates tensile failure, and SF indicates shear failure.

bank failure (characterized by TF in the middle and on the top and little SF at the toe). Since the failure region is almost TF, the failure pattern should be clarified as "toppling."

For bank collapse with large bank height (e.g., bank height = 1 m, Figure 5b), the pattern of the initial stress distribution agrees well with the one shown in Figure 5a (but with larger magnitudes). The failure pattern is characterized by SF at the bank toe (Stage I), TF at the bank top (Stage II), and sectional cracking from bank top to the toe (Stage III). The major differences between the aforementioned failure patterns can be summarized as follows. First, the larger the bank height, the larger σ_1' and σ_3' the bank toe will bear. As a result, in the context of bank collapse with small bank height, nearly no SF is detected at the bank toe when bank collapse occurs. Second, for bank collapse with large bank height, TF is first present on the bank top resulting from the SF at the bank toe. While in the context of bank collapse with small bank height, TF is first reached in the middle of the bank.
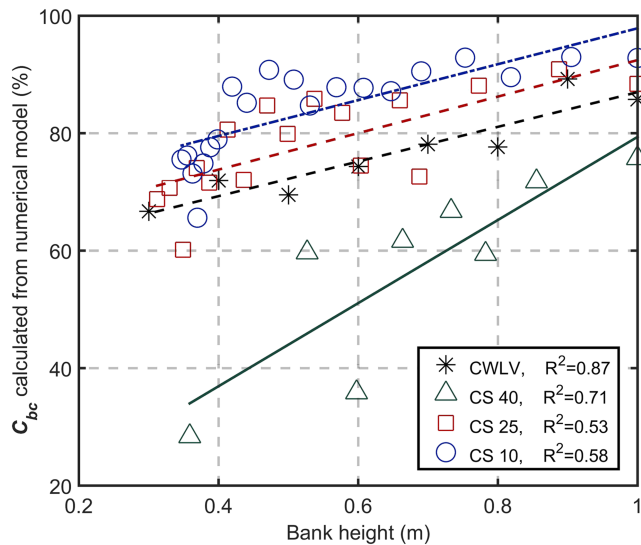
Figure 6. Relation between the calculated C_{bc} and the corresponding bank height. CWLV represents the numerical experiment with constant water level and flow velocity.

The relation between bank height and the calculated C_{bc} is shown in Figure 6. To separate the influences of variations in water level and topography, a specific numerical experiment is performed with constant water level (half of the bank height, corresponds to CS 40 in Figure 7b) and flow velocity (black asterisk in Figure 6). A significant linear relation is observed between bank height and C_{bc}, with correlation coefficient (R^2) up to 0.87 (black dashed line in Figure 6). Bank erosion occurs more frequently in the seaward part of the channel, resulting in massive bank collapse and consequent collapsed bank soil. This could be related to the observed increase of the meandering pattern (increase of the meander frequency and degree of sinuosity) at the mouth of tidal creeks, especially when there is a higher slope on this sector of the flat (see Figure 6.4d in Perillo et al., 2018). The collapsed bank soil then turns into bank toe thus reducing the bank height. Therefore, a landward increase in the occurrence of bank collapse is present. A monotonic trend suitable for all three CSs is detected with C_{bc} increasing as a function of bank height, indicating a decrease in bank stability. Taking CS 40, for example, C_{bc} reduces from 78% when bank height is 1 m to 31% when bank height is 0.38 m. Moreover, a significant linear correlation between C_{bc} and bank height is found near the channel mouth (for CS 40, R^2 can be up to 0.71). Near the landward boundary (e.g., CS 10), R^2 decreases sharply to 0.58, suggesting that C_{bc} is also subject to other factors. While the trend is clear for the most simplified case (constant water level and velocity, see *CWLV* in Figure 6), in all other cases (CS 10, CS 25, and CS 40) deviations from a perfect linear relation are present and result from the different types of failure and shape of the bank (e.g., small changes in a vertical bank result in relatively larger C_{bc} than for the case of a cantilever-shape bank). A landward decrease in the slope of the fitted line is also evident, indicating the weakening influences of bank height on C_{bc}. After comparing each CS, a monotonic increasing trend is found between the magnitude of C_{bc} and the distance to the open boundary. This indicates different types of bank failure resulting from specific flow patterns along the tidal channel (more details of the flow pattern are presented in section 3.3).

3.3. Near-Bank Flow Patterns and Resultant Bank Profile

The relation between near-bank water depth and bed shear stress over a tidal cycle is illustrated in Figure 7a. Close to the channel mouth (e.g., CS 40), the hydrodynamics are dominated by ebb currents with the absolute value of the maximum near-bank bed shear stress larger than 3 Pa (positive and negative sign indicate the flow direction). Near the landward boundary, CS 10, for example, the flood currents are characterized by
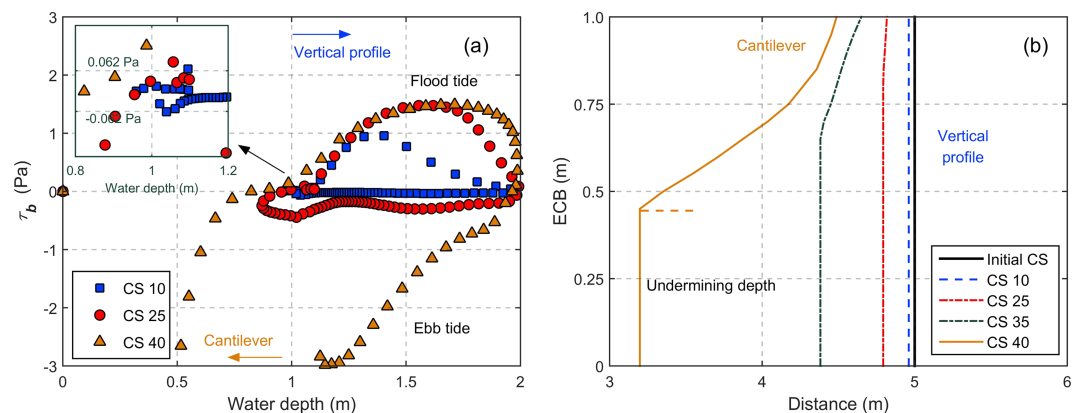

Figure 7. (a) Flow patterns showing the relation between water depth and the near-bank bed shear stress (τ_b) over a tidal cycle at year 0. The time interval between adjacent markers is 10 min. (b) The resultant bank profile after 10 tidal cycles with the assumption that no bank collapse occurs. The vertical axis ECB represents elevation with respect to channel bottom.

a maximum near-bank bed shear stress around 1 Pa. For CS 10, the duration of ebb tide is longer than 8 hr, and the absolute value of the near-bank bed shear stress is around the critical shear stress for bank erosion, τ_{be} (0.062 Pa in this case). In the context of CS 25 and CS 40, the duration of flood tide is slightly longer when compared to CS 10, with the near-bank bed shear stress mostly larger than τ_{be}. During the initial stage of the flood tide, a slightly landward decrease in near-bank bed shear stress is found along the tidal channel (i.e., water depth raises from 1 to 1.5 m). The near-bank bed shear stress subsequently decreases significantly near the landward boundary (e.g., water depth raises from 1.5 to 2 m). Contrary to CS 10, both CS 25 and CS 40 undergo a significant decrease in near-bank bed shear stress when approaching the maximum water depth. During the ebb tide, the maximum near-bank bed shear stress of each CS increases remarkably seaward due to a seaward increase in convergent flow from adjacent tidal flats.

The aforementioned near-bank flow patterns result in different shapes of the bank profile along the tidal channel, ranging gradually from vertical profile to cantilever shape (Figure 7b). The bank profile is simulated over 10 tidal cycles using initial topography with the assumption that no bank collapse occurs. Taking CS 10 as an example, the near-bank water level is higher than the elevation of bank top (i.e., near-bank water depth is higher than 1 m for initial topography) when the near-bank bed shear stress is larger than τ_{be}. Since the velocity variation in the vertical direction is neglected, vertically uniform bank erosion (from bank toe to the top) occurs, leading to a vertical profile (blue dash in Figure 7b). In the context of CS 25 and CS 40, however, the near-bank bed shear stress can be larger than τ_{be} no matter if the near-bank water level is higher than the elevation of bank top or not. The lower part of these banks undergoes bank erosion for longer, resulting in the occurrence of cantilever. No bank erosion can occur when the water level is below the undermining depth (UD). The smaller the minimum water depth below which bank erosion can occur, the smaller is the UD. Contrary to UW (Figure 4), a seaward decrease in UD is present.

3.4. Planimetric Evolution

Figure 8 shows the morphodynamic evolution of the tidal channel and adjacent tidal flats without bank erosion and collapse (Run A), without bank collapse (Run B1), and with both bank erosion and collapse (Run C1). The tidal channel is subject to remarkable erosion, while the neighboring tidal flats (around the 0-m contour line) undergo slight deposition. Since the tidal flow near the channel mouth (1 km from the open boundary) is ebb dominated (Figure 7a), net sediment transport is seaward. The seaward sediment deposits around the channel mouth as a result of a significant decrease in flow velocity, leading to the formation of an arched sand bar. This phenomenon is similar to sand bar formation in tidal inlet systems.

In the lower part of the tidal channel (near the open boundary), the channel depth continuously increases with decreasing deepening rate. In the upper part of the tidal channel (close to the landward boundary), the channel depth decreases during the first year (illustrated from the position of the −1-m contour line), as a consequence of a landward decrease in flow velocity and sufficient sediment resulting from bed/bank erosion in the lower part of the channel. Since bank soil is more vulnerable to erosion than bed soil (Kleinhans et al., 2009), more sediment is transported to the upper part of the tidal channel when bank erosion and/or collapse is considered, shallowing the upper part of the channel (i.e., −1-m contour line is far from the landward boundary). Subsequently, the upper part of the channel is subject to erosion resulting from flow contraction from year 2 to year 25, with the −1-m contour line approaching the landward boundary.

With respect to the width of the tidal channel, here illustrated using the 0-/−1-m contour line, in Run A, the tidal channel is narrowest since the tidal channel is characterized by deepening. Due to a landward decrease in bed shear stress (Figure 7a), the shape of the tidal channel is funneled (i.e., gradually decreasing in width landward) with its largest channel depth of around 5 m at year 25. When bank erosion is taken into account (Run B1), the shape of the tidal channel is also funneled but with larger channel width. Since the tidal channel is dominated by widening, the channel is shallower with its largest channel depth of around 4 m at year 25. Compared with Run B1, the tidal channel is narrower when bank collapse is considered (Run C1). Although accounting for bank collapse increases the rate of bank retreat, the collapsed bank soil depositing at the bank toe protects bank material from direct attacks and entrainments by the flow.
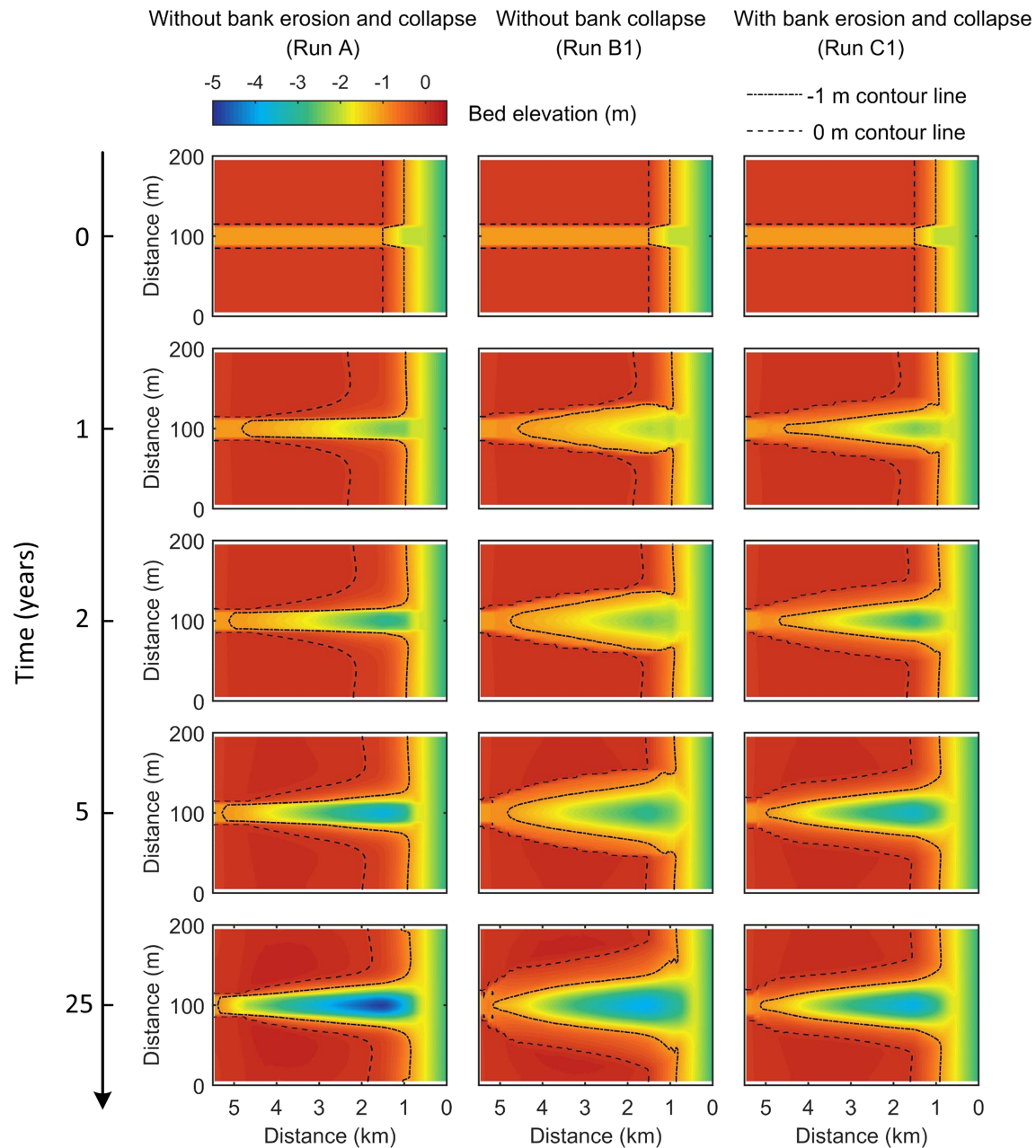
Figure 8. The morphodynamic evolution of the tidal channel and adjacent tidal flats without bank erosion and collapse (Run A), without bank collapse (Run B1), and with bank erosion and collapse (Run C1).

3.5. The Cross-Sectional Evolution of Tidal Channels

Figure 9 shows the morphodynamic evolution of three typical tidal channel CSs (CS 10, CS 25, and CS 40) in Run A, Run B1, and Run C1. A landward decrease is observed in tidal channel width and depth, and so in the resultant CS area, no matter if bank erosion and/or collapse is taken into account or not. Contrary to CS 40, the tidal flats region flanking the channel undergoes slight deposition in CS 10 and CS 25. This phenomenon is particularly evident at CS 10 when both bank erosion and collapse are neglected, leading to the formation of a "levee" (Figure 9o).

The initial abrupt bank gradually turns into a gentle slope in all runs but with different processes and consequently different shapes of the bank profile. The bank profile of Run A reaches a convex-shape as a consequence of bed erosion, when reaching the equilibrium state. In the context of Run B1, the smoothing
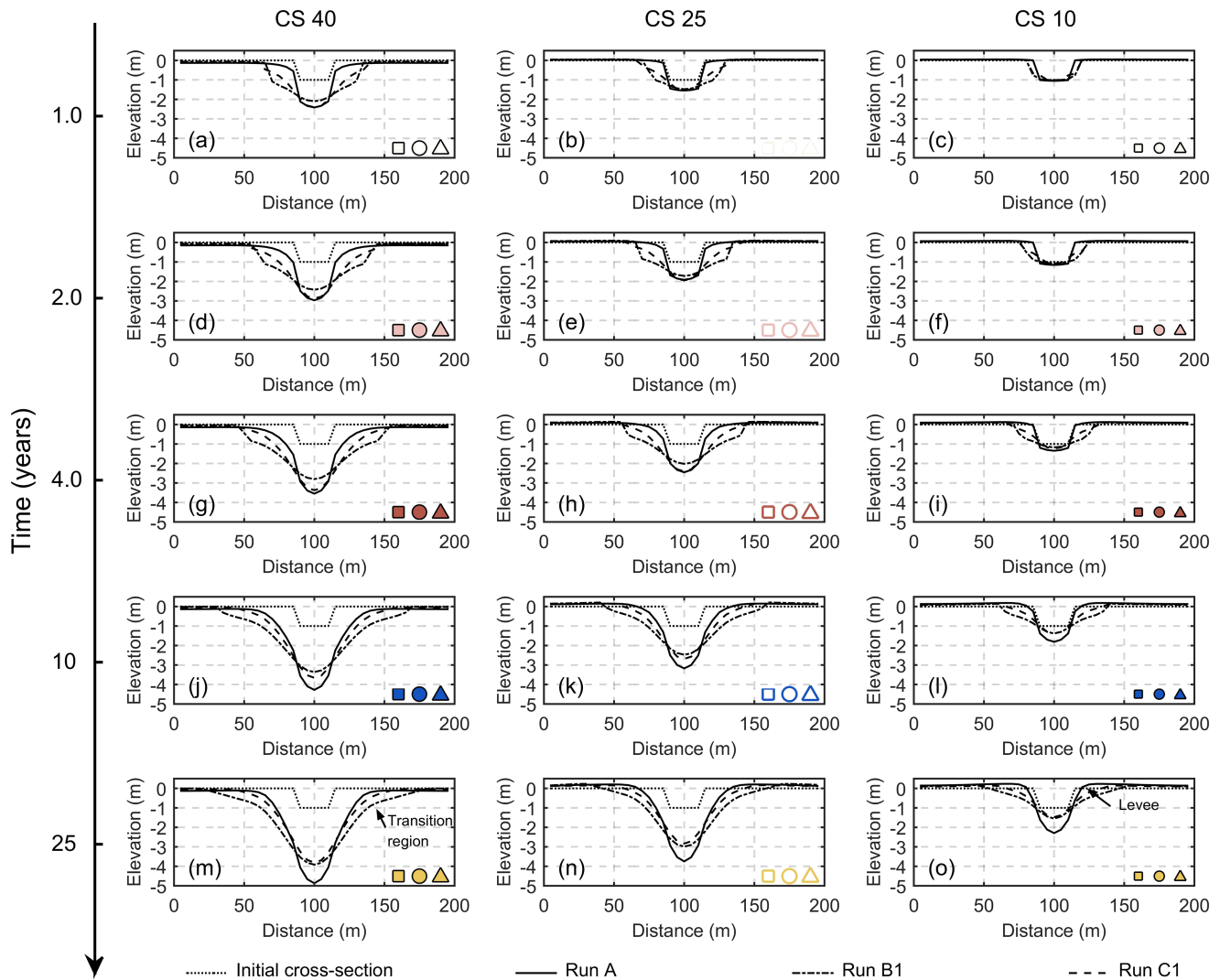
Figure 9. The morphodynamic evolution of three typical tidal channel cross sections (CS 40, CS 25, and CS 10) in Run A (without flow-induced bank erosion and collapse), Run B1 (without bank collapse) and Run C1 (with flow-induced bank erosion and collapse), respectively. The colored symbols in the right bottom corner of each subplot are used in Figure 14 to indicate the time and cross section number.

process depends on both the bed and bank erosion at the early stage, resulting in bank deformation in the transverse and vertical direction. Since bank soil is more vulnerable than bed soil, the bank profile of Run B1 is concave-shape for the first 4 years (dashed line in Figures 9a, 9d, and 9g). Subsequently, the cross-sectional evolution is subject to bed erosion; thus, the bank profile gradually turns into convex-shape as it approaches equilibrium. In Run C1, the transverse deformation of the bank profile is triggered by bank collapse. The collapsed bank soil depositing at the bank toe enhances vertical but weakens transverse deformation, leading to a convex-shape bank profile (dashed line in Figure 9j). The steepest bank slope is observed in Run A, while Run B1 undergoes the most gentle bank slope.

A transition region (TR) is found in Run B1, above which the bank slope decreases significantly (Figure 9m). It indicates that the channel CS evolution is driven by two processes: The upper part is mainly affected by bank erosion, while the lower part is subject to bed erosion. It is unexpected that no TR is presented in Run C1, showing a significant difference in CS shaping between flow-induced bank erosion and gravity-induced bank collapse.

Figure 10 shows the channel width and depth, width-to-depth ratio, and cross-sectional area as they gradually stabilize over time in Run A, Run B1, and Run C1, respectively (channel depth is evaluated by coupling
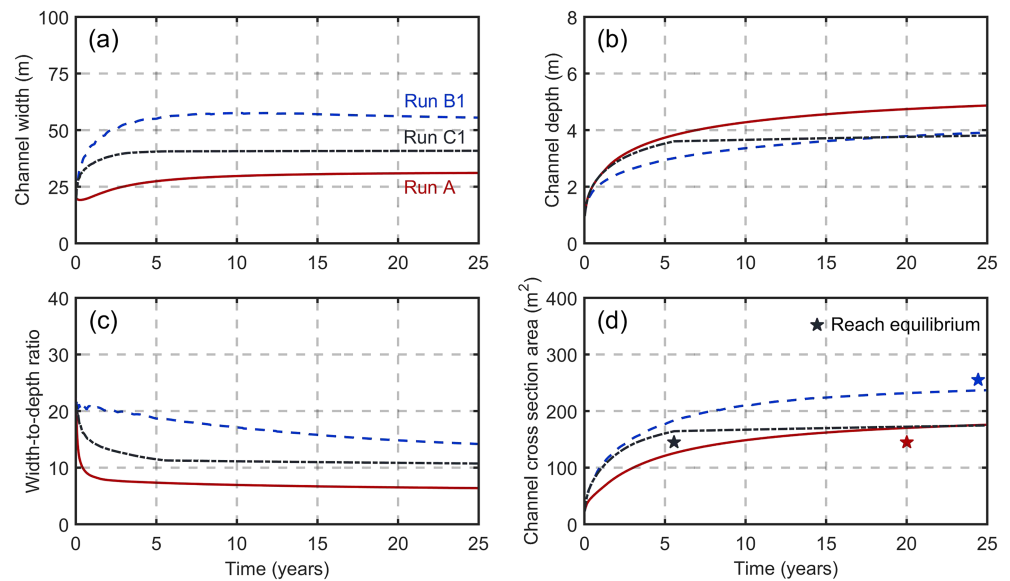
Figure 10. Time series of the (a) channel width and (b) depth, (c) width-to-depth ratio, and (d) channel cross-sectional area of CS 40 for Run A, Run B1, and Run C1, respectively. Pentagram indicates the time to reach the equilibrium state.

the bed elevation and the curvature threshold criteria, in analogy with Fagherazzi et al., 1999, while channel width is defined as the cross-sectional area divided by channel depth (Leopold et al., 1993)). When both bank erosion and collapse are neglected (Run A), the channel CS undergoes the smallest channel width, width-to-depth ratio and cross-sectional area but with the largest channel depth. In contrast, the largest channel width, width-to-depth ratio and cross-sectional area are found in Run B1. Contrary to Run C1, a wider but shallower CS is found in Run B1 during the first 5 years. Subsequently, the channel deepening rate of Run C1 decreases to 0, and the maximum CS depth in Run B1 gradually exceeds the one observed in Run C1 (Figure 10d). When reaching the equilibrium state, the channel depth in Run C1 is the smallest. A continuous cross-sectional expansion is found in Run B1 (Figure 10d), while Run A undergoes significant deepening (Figure 10b). It takes the shortest time to reach the equilibrium state when bank collapse is considered (Run C1, see Figure 10d), since bank collapse significantly increases the rate of channel expansion. The bank retreat process in Run C1 is observed only at the early stage (0–2 years, see Figure 10a), then the CS deepens slowly.
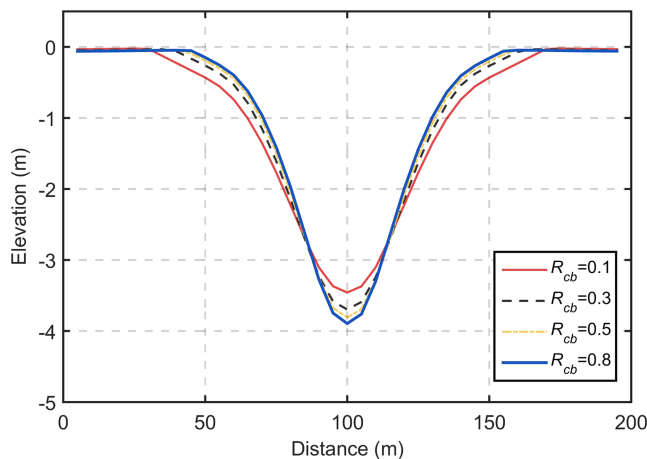

Figure 11. The influence of the ratio of collapsed bank soil translated into channel bed (R_{cb}) on the equilibrium morphology of tidal channel cross section (CS 40), with R_{cb} = 0.1 (Run C4), 0.3 (Run C5), 0.5 (Run C1), and 0.8 (Run C6).

Figure 11 shows the influence of R_{cb} (the ratio of collapsed bank soil translated into channel bed) on the equilibrium morphology of a typical tidal channel CS (CS 40), with R_{cb} = 0.1 (Run C4), 0.3 (Run C5), 0.5 (Run C1), and 0.8 (Run C6), respectively, and the relation between channel width, channel depth, and cross-sectional area at year 25. Although R_{cb} increases gradually from 0.1 to 0.8, the bank profile remains convex when reaching the equilibrium state. An increase in channel depth is found with the increase in R_{cb}. As expected, channel width reduces significantly by increasing R_{cb}.

Figure 12 shows the evolution of the tidal channel CS from a width-to-depth ratio perspective. The wedge slope in Figure 12 shows the ratio of the rate of channel widening to deepening (R_{wd}). A large R_{wd} (e.g., more than 10) indicates that the extension of the CS is subject to transverse bank retreat. Given that the deepening-induced increase in CS area can lead to an increase in channel width, a relatively small R_{wd} (e.g., less than 5) shows that the cross-sectional extension is dominated by vertical bed erosion. On the basis of R_{wd}, the evolution of a tidal channel CS can be categorized into three stages. During Stage I (0–5 years), a large R_{wd} with a landward increase tendency
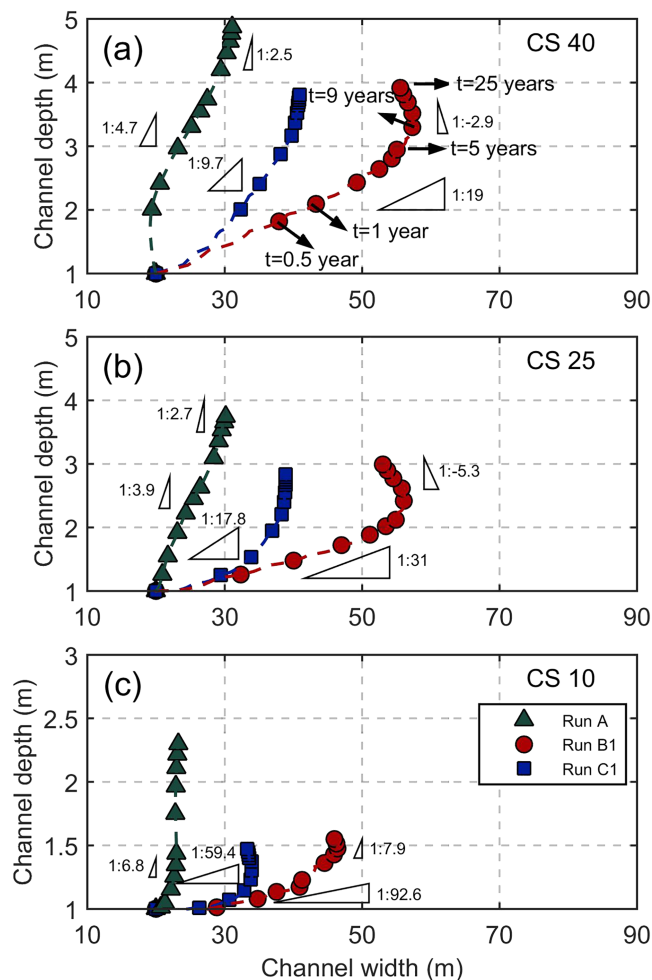
Figure 12. The relation between channel width and depth of three typical cross sections (CS 40, CS 25, and CS 10) with time. The wedge slope represents the ratio of the rate of channel widening to deepening (R_{wd}). A negative value of wedge slope means a decrease in channel width.

is found especially in Run B1 (e.g., R_{wd} reaches up to 92.6 in CS 10) and Run C1, indicating that the cross-sectional extension is characterized by widening. Including bank erosion significantly accelerates R_{wd} (e.g., R_{wd} increases from 4.7 to 19 in CS 40), while taking into account bank collapse reduces R_{wd} (e.g. R_{wd} decreases from 19 to 9.7 in CS 40). During Stage II (5–20 years), R_{wd} shows a significant decrease in all CSs and the maximum downtrend occurs at CS 10 (reduce 90% from 92.6 to 7.9). An inflection point is observed in the three CSs in Run B1, showing that R_{wd} decreases to a negative value. In other words, channel width decreases with the increase in channel depth. We observe a TR (Figure 9m) characterized by a significant increase in deposition, leading to a decrease in cross-sectional area and resultant channel width. During Stage III (20–25 years), the absolute value of R_{wd} gradually approaches 0, indicating a slow-varying or even constant channel depth and width.

4. Discussion

The influences of collapsed bank soil on bank collapse patterns and the morphodynamic evolution of tidal channels have been analyzed using a numerical model. We have investigated quantitatively the effect of bank height on bank collapse and the contribution of bank collapse to bank retreat (C_{bc}). We have also analyzed how the planimetric and cross-sectional evolution of tidal channels is affected by the collapsed bank soil.

In order to gain more insight, we highlight the following three questions: (1) What factors may affect the process of bank collapse and the associated failure patterns in tidal systems? (2) What role the collapsed bank soil plays in the morphodynamic evolution of tidal channels? (3) Is the simulated width-to-depth ratio comparable with the natural one?

4.1. Bank Collapse in Tidal Systems

As a consequence of different primary drivers of the flow motion (Bayliss-Smith et al., 1979; Coco et al., 2013), bank collapse in tidal systems is more complicated than its fluvial counterpart, which has been extensively studied over the last four decades (Darby et al., 2007; Deng et al., 2018; Simon et al., 2000; Stecca et al., 2017; Thorne, 1982). Three factors, resulting in the differences in bank collapse between tidal and fluvial system, are bank height, bank profile shape, and the transition between saturated and unsaturated soil. As shown in section 3.2, the failure patterns and consequent C_{bc} are significantly affected by bank height because (1) bank collapse with large bank height is characterized by shear failure (SF) at the bank toe and tensile failure (TF) at the bank top, while bank collapse with small bank height is subject to TF (Figure 5) and (2) a higher C_{bc} is present with an increase in bank height (Figure 6). On one hand, the funnel-shape tidal channel and estuary (Gong et al., 2018; Lanzoni & D'Alpaos, 2015; van der Wegen et al., 2008) undergoes a landward decrease in channel width and depth (Figure 8) and so the cross-sectional area (Figure 9), possibly leading to a seaward increase in bank height. Tidal flats are commonly dissected by intricate tidal networks with apple tree shapes (Coco et al., 2013; D'Alpaos, 2005) where a smaller cross-sectional area, as well as consequently bank height, is expected for the branches. On the other hand, since tidal channels are commonly characterized by meandering and cutoff (Marani et al., 2002; Solari et al., 2002), the bank height of tidal channels shows significant differences even in the same region.

Friedrichs and Aubrey (1988) stated that frictional interaction between the tide and channel bottom causes relatively shorter floods and resultant larger flow velocity (flood dominated), while intertidal storage leads to relatively shorter ebbs and consequently strong current velocity (ebb dominated). In the context of a flood-dominated tide (e.g., CS 10 in Figure 7a), the bed shear stress τ_b exceeds the critical shear stress for bank erosion τ_{be} with relatively large water depth, resulting in a vertical bank profile (blue dashed line in Figure 7b).
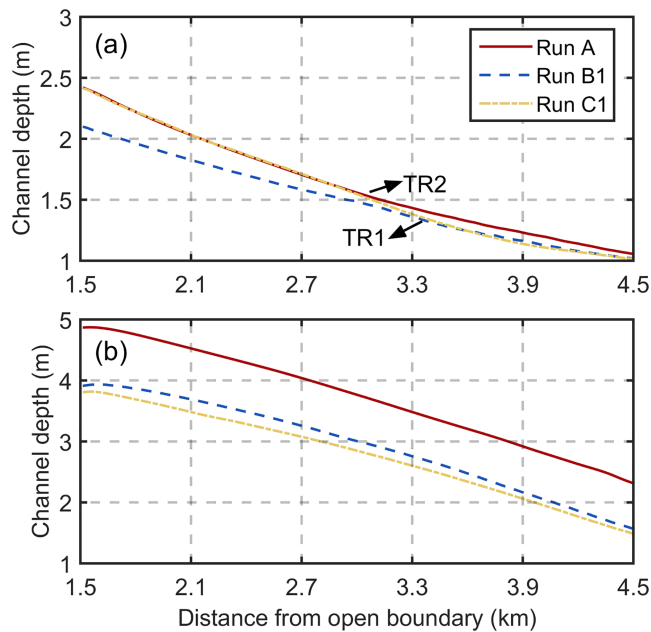
Figure 13. The tidal channel depth in talweg (extracted from Figure 8) after 1 (a) and 25 (b) years.

For an ebb-dominated tide (e.g., CS 40 in Figure 7a), τ_b is larger than τ_{be} when water depth is relatively low, leading to a cantilever-shape bank (yellow line in Figure 7b). The failure patterns and resultant C_{bc} of bank collapse can be remarkably influenced by the shape of the bank profile (e.g., UD and UW). The failure pattern of bank collapse with relatively small UD is characterized by SF at the bank toe and TF on the bank top (Figure 5a). By increasing the UD, SF at the bank toe is absent and bank collapse is induced by TF in the middle and upper part of the bank (Figures 4b and 4c). Moreover, the UD and UW increase gradually seaward (Figure 7b), indicating that more bank erosion is needed to trigger bank collapse. Therefore, a landward increase in C_{bc} is observed (Figure 6).

In terms of model limitations, results of Gong et al. (2018) show that the loss of hydrostatic pressure during ebb tide promotes the occurrence of bank collapse, consistent with Simon et al. (2000). However, Deng et al. (2018) argued that pore water pressure resulting from the transition between saturated and unsaturated soil rather than hydrostatic pressure triggers bank failure. The increased pore water pressure resulting from rapid decrease in channel water level significantly weakens bank stability. Given that the recession of tidal stage is quicker and more frequent than river stage, it is worthwhile taking into account the variation in water pore pressure. Besides, sediment sorting may potentially lead to a landward decrease in sediment grain size (Zhou, Ye, et al., 2016). A larger sediment grain size usually accounts for a larger permeability coefficient, relating to the pore water pressure after tidal stage recession. We leave inclusion of these processes for future studies.

4.2. The Role of Collapsed Bank Soil on Tidal Channel Evolution

Flow-induced bank erosion and consequent collapse result in significant sediment redistribution in tidal systems. On one hand, the soil of the channel bank is more vulnerable than bed soil. Under the action of tidal currents and/or waves, the eroded bank soil transforming into suspended sediment is diffused around the whole region, leading to morphological changes well beyond the original source. On the other hand, collapsed bank soil instantaneously depositing at the bank toe causes local morphological change. The two processes can trigger morphological variations in both longitudinal and transverse directions of tidal channels. Figure 13 shows the tidal channel depth in the talweg at 1 and 25 years, respectively. During the first year, significant differences in tidal channel depth are observed between Run A and Run B1. Without bank erosion and collapse the tidal channel is subject to deepening, while the tidal channel is dominated by widening when bank erosion is taken into account. Therefore, the channel depth in Run A is longitudinally larger than the channel depth in Run B1. When bank collapse is considered, the collapsed bank soil may directly deposit at the bank toe thus weakening the process of channel widening. Two obvious TRs are found with TR1 between Run B1 and Run C1 and TR2 between Run A and Run C1 (Figure 13a). Close to the landward boundary, infrequent bank collapse resulting from weak tidal currents leads to similar channel bed profile between Run B1 and Run C1, thus forming TR1. In contrast, bank collapse occurs frequently near the channel mouth because of strong tidal currents, resulting in the formation of TR2. At year 25, a remarkable difference is observed between each case, indicating the role of flow-induced bank erosion and the collapsed bank soil on the longitudinal morphology of the tidal channel.

The influence of collapsed bank soil on the tidal channel morphology in the transverse direction can be investigated through the shape of the bank profile. In order to quantitatively depict the shape of the bank profile, B_s and B_m are defined herein as follows. B_s is the area of the tidal channel CS divided by the channel depth in the talweg; B_m is the distance between two points on the right and left bank profile, respectively, with their elevations being the average between the elevation of the bank top and the channel bed in the talweg. A quantitative description of the bank profile shape can be obtained by comparing B_s and B_m. If B_s is equal to B_m, a linear-shape bank profile is present (e.g., a rectangular shape or V shape); if B_s is larger than B_m, the bank profile is convex shape; a concave shape is found if B_s is smaller than B_m (e.g., U shape). The
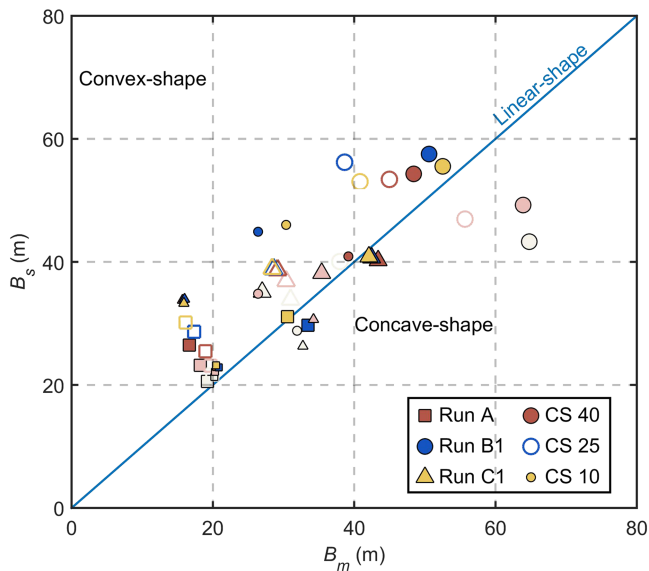
Figure 14. The relation between B_s and B_m. Each dot represents a simulation with a specific time and cross section number, and the type of simulation is indicated by the corresponding color and shape of the dots in Figure 9.

relation between B_s and B_m is shown in Figure 14. The large scatter indicates a significant difference in the shape of channel CS for each run. At the early stage of the tidal channel evolution (e.g., 0–2 years), the morphology of the channel CS is greatly influenced by the collapsed bank soil. Taking CS 40 as an example and looking at Figure 9, symbols representing Run B1 are below the 1:1 line, indicating a concave-shape CS (Figures 9a and 9d). In contrast, symbols representing Run A and Run C1 are above the 1:1 line, indicating a convex-shape CS (Figures 9a and 9d). When reaching equilibrium, all CS 40 runs are on the 1:1 line, indicating a linear-shape bank profile. The effects of the collapsed bank soil on the cross-sectional morphology of channels is also affected by the position of the CS. Contrary to the linear-shape CS observed toward the seaside, the CS is more convex when approaching the landside.

4.3. Comparison With Natural Systems

This research investigates the role of collapsed bank soil on the morphology of tidal channels under the action of tidal currents. In order to compare simulated and natural tidal channels, tidal flat channels from lagoon environmental settings are chosen. Figure 15 shows the simulated channel width-to-depth ratio at year 25 and field data derived from measurements of tidal channels around the world (Garofalo, 1980; Leopold et al., 1993; Marani et al., 2002; Williams et al., 2002). The tidal regime in Venice Lagoon is mesotidal (2–4 m) and semidiurnal, consistent with the hydrodynamic conditions employed in this study (tidal range is set to 2 m). Besides, critical shear stress for bed erosion (0.5 Pa), the erosion parameter for bed erosion (5×10^{-5} kg/m^2/s) and settling velocity (5×10^{-4} m/s) used in this study are of the same order of magnitude of previous studies on Venice Lagoon (D'Alpaos, 2005; Fagherazzi & Furbish, 2001; Lanzoni & D'Alpaos, 2015). The simulated width-to-depth ratio shows a good agreement with natural observations. Changes in the parameters (e.g., R_{cb}) affect the width-depth ratio, but for the chosen parameter space all simulations result in channel geometry (i.e., width-to-depth ratio) that are consistent with the observations. Observations of width-to-depth ratio can only indicate consistency in long-term behavior and are not likely to distinguish between cases where bank collapse is dominant or not. The width of the
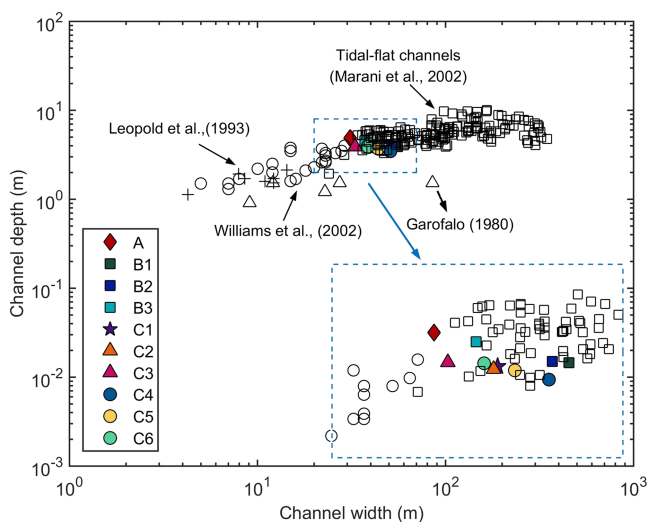

Figure 15. Simulated channel width to depth at year 25 and field data derived from measurements of tidal channels in New Jersey, USA (Garofalo, 1980), San Francisco Bay, USA (Leopold et al., 1993; Williams et al., 2002), and the Venice Lagoon, Italy (Marani et al., 2002). Run ID corresponds to Table 3.

equilibrium section is larger when bank collapse is neglected (Figures 12 and 15), but the difference is small and difficult to detect in observations where natural variability plays a bigger role. On the other hand, our numerical simulations indicate that, while the morphology adjusts toward the equilibrium configuration, the cross-sectional profile is convex when bank collapse is considered and concave when neglected (Figure 9). Also, because of the "protection" effect, the CS experiences less erosion when bank collapse is included.

The occurrence of bank erosion and collapse favors widening of tidal channels. Given that a correlation is present between the cross-sectional area and the tidal prism (i.e., *P-A* relationship; O'Brien, 1931; Jarrett, 1976), an increase in channel width should result in a decrease in channel depth. However, for natural tidal channels the relation between channel width and depth is nonlinear. First, wind waves and large gradients in topography may increase local bed shear stress and the resultant cross-sectional area. Second, the heterogeneity of bank soil in both the longitudinal and the transverse direction can lead to different ratios between channel width and depth even under the same prescribed hydrodynamic conditions. In order to better understand the morphodynamic evolution of tidal channels in natural systems, some neglected physical processes need to be incorporated in the present model. To start with, bed load transport is needed to better address the transport of collapsed sediment.

Second, wind waves enhance local bed shear stress, thus leading to more frequent occurrences of bank collapse. Finally, the influence of vegetation root systems on bank stability should be incorporated to investigate the difference in bank collapse between bare flats and salt marshes.

5. Conclusion

On the basis of Gong et al. (2018), a process-based geomorphodynamic model able to study the morphodynamic evolution of tidal channels is presented, providing new insight on the collapsed bank soil affecting the overall channel geometry at equilibrium. Despite several assumptions needed to simplify the coupling between bank collapse and bed level change, the model reproduces failure patterns of bank collapse and several observed channel characteristics of geomorphic relevance.

In the context of bank collapse with small bank height, shear failure (SF) is absent, and tensile failure (TF) in the middle of the bank (Stage I), TF on the bank top (Stage II), and sectional cracking from bank top to the toe (Stage III) are present sequentially before bank collapse occurs. For bank collapse with large bank height, the failure pattern is characterized by SF at the bank toe (Stage I), TF at the bank top (Stage II), and sectional cracking from the bank top to the toe (Stage III). Since the failure region is almost TF, the failure pattern should be classified as toppling.

According to the validation against previous experiments, C_{bc} calculated from the proposed bank collapse module agrees well with that from laboratory experiments. A monotonic trend is detected with C_{bc} increasing as a function of bank height. Also, a monotonic increasing trend is present between the magnitude of C_{bc} and the distance to seaward boundary, indicating different types of bank failure resulting from specific flow patterns along the tidal channel.

The bank profile is linear or slightly convex, and the planimetric shape of tidal channels (gradually decreasing in width landward) is similar when approaching equilibrium regardless of the consideration of bank erosion and collapse. Since bank soil is more vulnerable than bed soil, channel width increases significantly when bank erosion is taken into account. Contrary to bank erosion, bank collapse prevents the widening process since the collapsed bank material protects the bank from direct bank erosion. The cross-sectional evolution of tidal channel is characterized by three stages: widening stage, deepening stage, and slow development stage.

Applying similar hydrodynamic and morphodynamic parameters, the simulated width-to-depth ratios agree well with the observations in Venice Lagoon. As more data become available, we will be able to test the model predictions over a broader range of conditions and so fully unravel the role of bank collapse on channel evolution.

References

Allen, J. (2000). Morphodynamics of Holocene salt marshes: A review sketch from the Atlantic and Southern North Sea coasts of Europe. *Quaternary Science Reviews*, *19*(12), 1155–1231.

Barbier, E. B., Hacker, S. D., Kennedy, C., Koch, E. W., Stier, A. C., & Silliman, B. R. (2011). The value of estuarine and coastal ecosystem services. *Ecological Monographs*, *81*(2), 169–193.

Bayliss-Smith, T. P., Healey, R., Lailey, R., Spencer, T., & Stoddart, D. R. (1979). Tidal flows in salt marsh creeks. *Estuarine and Coastal Marine Science*, *9*(3), 235–255.

Bendoni, M., Francalanci, S., Cappietti, L., & Solari, L. (2014). On salt marshes retreat: Experiments and modeling toppling failures induced by wind waves. *Journal of Geophysical Research: Earth Surface*, *119*, 603–620. https://doi.org/10.1002/2013JF002967

Canestrelli, A., Spruyt, A., Jagers, B., Slingerland, R., & Borsboom, M. (2016). A mass-conservative staggered immersed boundary model for solving the shallow water equations on complex geometries. *International Journal for Numerical Methods in Fluids*, *81*(3), 151–177.

Chen, Y., Thompson, C. E. L., & Collins, M. B. (2012). Saltmarsh creek bank stability: Biostabilisation and consolidation with depth. *Continental Shelf Research*, *35*, 64–74.

Chew, L. P. (1989). Constrained Delaunay triangulations. *Algorithmica*, *4*(1-4), 97–108.

Coco, G., Zhou, Z., van Maanen, B., Olabarrieta, M., Tinoco, R., & Townend, I. (2013). Morphodynamics of tidal networks: Advances and challenges. *Marine Geology*, *346*, 1–16.

D'Alpaos, A. (2005). Tidal network ontogeny: Channel initiation and early development. *Journal of Geophysical Research*, *110*, F02001. https://doi.org/10.1029/2004JF000182

D'Alpaos, A., Lanzoni, S., Marani, M., & Rinaldo, A. (2010). On the tidal prism–channel area relations. *Journal of Geophysical Research*, *115*, F01003. https://doi.org/10.1029/2008JF001243

Darby, S. E., Rinaldi, M., & Dapporto, S. (2007). Coupled simulations of fluvial erosion and mass wasting for cohesive river banks. *Journal of Geophysical Research*, *112*, F03022. https://doi.org/10.1029/2006JF000722

Deltares (2014). *Delft3D-FLOW: Simulation of multi-dimensional hydrodynamic flows and transport phenomena, including sediments—User manual* (369 pp). Delft, Netherlands: Deltares

Deng, S., Xia, J., Zhou, M., Li, J., & Zhu, Y. (2018). Coupled modeling of bank retreat processes in the Upper Jingjiang Reach, China. *Earth Surface Processes and Landforms*, *43*(14), 2863–2875. https://doi.org/10.1002/esp.4439

Fagherazzi, S., Bortoluzzi, A., Dietrich, W. E., Adami, A., Lanzoni, S., Marani, M., & Rinaldo, A. (1999). Tidal networks: 1. Automatic network extraction and preliminary scaling features from digital terrain maps. *Water Resources Research*, *35*(12), 3891–3904.

Fagherazzi, S., & Furbish, D. J. (2001). On the shape and widening of salt marsh creeks. *Journal of Geophysical Research*, *106*(C1), 991–1003.

Fagherazzi, S., Kirwan, M. L., Mudd, S. M., Guntenspergen, G. R., Temmerman, S., D'Alpaos, A., et al. (2012). Numerical models of salt marsh evolution: Ecological, geomorphic, and climatic factors. *Reviews of Geophysics*, *50*, RG1002. https://doi.org/10.1029/2011RG000359

Fox, G. A., & Felice, R. G. (2014). Bank undercutting and tension failure by groundwater seepage: Predicting failure mechanisms. *Earth Surface Processes and Landforms*, *39*(6), 758–765.

Fox, G. A., & Wilson, G. V. (2010). The role of subsurface flow in hillslope and stream bank erosion: A review. *Soil Science Society of America Journal*, *74*(3), 717–733.

Francalanci, S., Bendoni, M., Rinaldi, M., & Solari, L. (2013). Ecomorphodynamic evolution of salt marshes: Experimental observations of bank retreat processes. *Geomorphology*, *195*(Supplement C), 53–65.

Friedrichs, C. T. (1995). Stability shear stress and equilibrium cross-sectional geometry of sheltered tidal channels. *Journal of Coastal Research*, 1062–1074.

Friedrichs, C. T. (2011). 3.06-Tidal flat morphodynamics: A synthesis. In *Treatise on Estuarine and Coastal Science* (pp. 137–170). Waltham: Academic Press.

Friedrichs, C. T., & Aubrey, D. G. (1988). Non-linear tidal distortion in shallow well-mixed estuaries: A synthesis. *Estuarine, Coastal and Shelf Science*, *27*(5), 521–545.

Gabet, E. J. (1998). Lateral migration and bank erosion in a saltmarsh tidal channel in San Francisco Bay, California. *Estuaries and Coasts*, *21*(4), 745–753.

Garofalo, D. (1980). The influence of wetland vegetation on tidal stream channel migration and morphology. *Estuaries*, *3*(4), 258–270.

Ginsberg, S. S., & Perillo, G. M. E. (1990). Channel bank recession in the Bahía Blanca estuary, Argentina. *Journal of Coastal Research*, 999–1009.

Gong, Z., Jin, C., Zhang, C., Zhou, Z., Zhang, Q., & Li, H. (2017). Temporal and spatial morphological variations along a cross-shore intertidal profile, Jiangsu, China. *Continental Shelf Research*, *144*, 1–9.

Gong, Z., Zhao, K., Zhang, C., Dai, W., Coco, G., & Zhou, Z. (2018). The role of bank collapse on tidal creek ontogeny: A novel process-based model for bank retreat. *Geomorphology*, *311*, 13–26.

Hanson, G. J., & Simon, A. (2001). Erodibility of cohesive streambeds in the loess area of the midwestern USA. *Hydrological Processes*, *15*(1), 23–38.

Ikeda, S., Parker, G., & Kimura, Y. (1988). Stable width and depth of straight gravel rivers with heterogeneous bed materials. *Water Resources Research*, *24*(5), 713–722.

Jarrett, J. T. (1976). Tidal prism-inlet area relationships, edited, Army Engineer Waterways Experiment Station Vicksburg Miss.

Karmaker, T., & Dutta, S. (2013). Modeling seepage erosion and bank retreat in a composite river bank. *Journal of Hydrology*, *476*, 178–187.

Kirwan, M. L., & Murray, A. B. (2007). A coupled geomorphic and ecological model of tidal marsh evolution. *Proceedings of the National Academy of Sciences*, *104*(15), 6118–6122.

Kleinhans, M. G., Schuurman, F., Bakx, W., & Markies, H. (2009). Meandering channel dynamics in highly cohesive sediment on an intertidal mud flat in the Westerschelde estuary, the Netherlands. *Geomorphology*, *105*(3), 261–276.

Krone, R. B. (1962). Flume studies of the transport of sediment in estuarial shoaling processes, final report, Hydraul, *Eng. Lab. and Sanit. Eng. Res. Lab., Univ. of Calif., Berkeley*.

Lai, Y. G., Thomas, R. E., Ozeren, Y., Simon, A., Greimann, B. P., & Wu, K. (2015). Modeling of multilayer cohesive bank erosion with a coupled bank stability and mobile-bed model. *Geomorphology*, *243*, 116–129.

Langendoen, E. J. (2000). Concepts: Conservational channel evolution and pollutant transport system, USDA-ARS Naitonal Sedimentation Laboratory.

Lanzoni, S. (2002). Long-term evolution and morphodynamic equilibrium of tidal channels. *Journal of Geophysical Research*, *107*(C1), 3001. https://doi.org/10.1029/2000JC000468

Lanzoni, S., & D'Alpaos, A. (2015). On funneling of tidal channels. *Journal of Geophysical Research: Earth Surface*, *120*, 433–452. https://doi.org/10.1002/2014JF003203

Larsen, L. G., Harvey, J. W., & Crimaldi, J. P. (2007). A delicate balance: Ecohydrological feedbacks governing landscape morphology in a lotic peatland. *Ecological Monographs*, *77*(4), 591–614.

Leopold, L. B., Collins, J. N., & Collins, L. M. (1993). Hydrology of some tidal channels in estuarine marshland near San Francisco. *Catena*, *20*(5), 469–493.

Lindow, N., Fox, G. A., & Evans, R. O. (2009). Seepage erosion in layered stream bank material. *Earth Surface Processes and Landforms*, *12*(34), 1693–1701.

Marani, M., Lanzoni, S., Zandolin, D., Seminara, G., & Rinaldo, A. (2002). Tidal meanders. *Water Resources Research*, *38*(11), 1225. https://doi.org/10.1029/2001WR000404

Mariotti, G., Kearney, W. S., & Fagherazzi, S. (2016). Soil creep in salt marshes. *Geology*, *44*(6), 459–462.

Nardi, L., Rinaldi, M., & Solari, L. (2012). An experimental investigation on mass failures occurring in a riverbank composed of sandy gravel. *Geomorphology*, *163-164*, 56–69.

O'Brien, M. P. (1931). Estuary tidal prisms related to entrance areas. *Civil Engineering*, *1*, 738–739.

Parker, G. (1978). Self-formed straight rivers with equilibrium banks and mobile bed. Part 2. The gravel river. *Journal of Fluid Mechanics*, *89*(1), 127–146.

Partheniades, E. (1965). Erosion and deposition of cohesive soils. *Journal of the Hydraulics Division*, *91*(1), 105–139.

Patsinghasanee, S., Kimura, I., Shimizu, Y., & Nabi, M. (2018). Experiments and modelling of cantilever failures for cohesive riverbanks. *Journal of Hydraulic Research*, *56*(1), 76–95. https://doi.org/10.1080/00221686.2017.1300194

Perillo, G. M. E. (2009). Tidal courses: Classification, origin and functionality. In *Coastal Wetlands: An Integrated Ecosystem Approach* (pp. 185–209). Amsterdam: Elsevier.

Perillo, G. M. E., Wolanski, E., Cahoon, D. R., & Hopkinson, C. S. (2018). *Coastal wetlands: An integrated ecosystem approach*. Amsterdam: Elsevier.

Pizzuto, J. E. (1990). Numerical simulation of gravel river widening. *Water Resources Research*, *26*(9), 1971–1980.

Rinaldi, M., & Darby, S. E. (2007). 9 Modelling river-bank-erosion processes and mass failure mechanisms: Progress towards fully coupled simulations. *Developments in Earth Surface Processes*, *11*, 213–239.

Roelvink, J. A. (2006). Coastal morphodynamic evolution techniques. *Coastal Engineering*, *53*(2-3), 277–287.

Samadi, A., Amiri-Tokaldany, E., Davoudi, M. H., & Darby, S. E. (2013). Experimental and numerical investigation of the stability of overhanging riverbanks. *Geomorphology*, *184*, 1–19.

Samadi, S., Davoudi, M. H., & Amiri-Tokaldany, E. (2011). Experimental study of cantilever failure in the upper part of cohesive riverbanks. *Research Journal of Environmental Sciences*, *5*(5), 444.

Simon, A., Curini, A., Darby, S. E., & Langendoen, E. J. (2000). Bank and near-bank processes in an incised channel. *Geomorphology*, *35*(3–4), 193–217.

Simon, A., & Thomas, R. E. (2002). Processes and forms of an unstable alluvial system with resistant, cohesive streambeds. *Earth Surface Processes and Landforms*, *27*(7), 699–718.

Solari, L., Lanzoni, S., Marani, M., & Rinaldo, A. (2002). Sand bars in tidal channels Part 2. Tidal meanders. *Journal of Fluid Mechanics*, *451*, 203–238. https://doi.org/10.1017/S0022112001006565

Stecca, G., Measures, R., & Hicks, D. M. (2017). A framework for the analysis of noncohesive bank erosion algorithms in morphodynamic modeling. *Water Resources Research*, *53*, 6663–6686. https://doi.org/10.1002/2017WR020756

Thorne, C. R. (1982). Processes and mechanisms of river bank erosion. *Gravel-bed Rivers*, 227–259.

van der Wegen, M., Dastgheib, A., & Roelvink, J. A. (2010). Morphodynamic modeling of tidal channel evolution in comparison to empirical PA relationship. *Coastal Engineering*, *57*(9), 827–837.

van der Wegen, M., & Roelvink, J. A. (2008). Long-term morphodynamic evolution of a tidal embayment using a two-dimensional, process-based model. *Journal of Geophysical Research*, *113*, C03016. https://doi.org/10.1029/2006JC003983

van der Wegen, M., Wang, Z. B., Savenije, H. H. G., & Roelvink, J. A. (2008). Long-term morphodynamic evolution and energy dissipation in a coastal plain, tidal embayment. *Journal of Geophysical Research*, *113*, F03001. https://doi.org/10.1029/2007JF000898

Van Eerdt, M. M. (1985). Salt marsh cliff stability in the Oosterschelde. *Earth Surface Processes and Landforms*, *10*(2), 95–106.

van Maanen, B., Coco, G., & Bryan, K. R. (2015). *On the ecogeomorphological feedbacks that control tidal channel network evolution in a sandy mangrove setting*. London: The Royal Society. 2015-01-01

Williams, P. B., Orr, M. K., & Garrity, N. J. (2002). Hydraulic geometry: A geomorphic design tool for tidal marsh channel evolution in wetland restoration projects. *Restoration Ecology*, *10*(3), 577–590.

Xu, F., Coco, G., Tao, J., Zhou, Z., Zhang, C., Lanzoni, S., & D'Alpaos, A. (2019). On the morphodynamic equilibrium of a short tidal channel. *Journal of Geophysical Research: Earth Surface*, *124*, 639–665. https://doi.org/10.1029/2018JF004952

Xu, F., Coco, G., Zhou, Z., Tao, J., & Zhang, C. (2017). A numerical study of equilibrium states in tidal network morphodynamics. *Ocean Dynamics*, *12*(67), 1593–1607.

Zhou, Z., Olabarrieta, M., Stefanon, L., D'Alpaos, A., Carniello, L., & Coco, G. (2014). A comparative study of physical and numerical modeling of tidal network ontogeny. *Journal of Geophysical Research: Earth Surface*, *119*, 892–912. https://doi.org/10.1002/2014JF003092

Zhou, Z., van der Wegen, M., Jagers, B., & Coco, G. (2016). Modelling the role of self-weight consolidation on the morphodynamics of accretional mudflats. *Environmental Modelling and Software*, *76*, 167–181.

Zhou, Z., Ye, Q., & Coco, G. (2016). A one-dimensional biomorphodynamic model of tidal flats: Sediment sorting, marsh distribution, and carbon accumulation under sea level rise. *Advances in Water Resources*, *93*, 288–302.